Accepted Manuscript

Marine sulfur cycle evidence for upwelling and eutrophic stresses during early triassic cooling events

Alan Stebbins, Thomas J. Algeo, Leopold Krystyn, Harold Rowe, Michael Brookfield, Jeremy Williams, Steven W. Nye, Robyn Hannigan

PII: S0012-8252(18)30103-X

DOI: doi:10.1016/j.earscirev.2018.09.007

Reference: EARTH 2696

To appear in: Earth-Science Reviews

Received date: 16 February 2018
Revised date: 30 August 2018
Accepted date: 12 September 2018

Please cite this article as: Alan Stebbins, Thomas J. Algeo, Leopold Krystyn, Harold Rowe, Michael Brookfield, Jeremy Williams, Steven W. Nye, Robyn Hannigan, Marine sulfur cycle evidence for upwelling and eutrophic stresses during early triassic cooling events. Earth (2018), doi:10.1016/j.earscirev.2018.09.007

This is a PDF file of an unedited manuscript that has been accepted for publication. As a service to our customers we are providing this early version of the manuscript. The manuscript will undergo copyediting, typesetting, and review of the resulting proof before it is published in its final form. Please note that during the production process errors may be discovered which could affect the content, and all legal disclaimers that apply to the journal pertain.



Marine sulfur cycle evidence for upwelling and eutrophic stresses during Early Triassic cooling events

Alan Stebbins^{a*}, Thomas J. Algeo^{b,c}, Leopold Krystyn^d, Harold Rowe^e, Michael Brookfield^a, Jeremy Williams^f, Steven W. Nye Jr^a and Robyn Hannigan^a

- a. School for the Environment, University of Massachusetts Boston, Boston, MA 02125,
 USA
- b. Department of Geology, University of Cincinnati, Cincinnati, OH 45221, USA
- c. State Key Laboratories of BGEG and GPMR, China University of Geosciences, Wuhan 430074, China
- d. Institute for Paleontology, Vienna University, Althanstrasse 14, 1090 Vienna, Austria
- e. Bureau of Economic Geology, The University of Texas at Austin, Austin, TX, 78758 USA
- f. Department of Geology, Kent State University, Kent, OH 44242, USA
- * Corresponding author: alan.stebbins001@umb.edu

Abstract

Perturbations to the global carbon and sulfur cycles recurred episodically throughout the ~5-Myr-long Early Triassic, in the aftermath of the end-Permian mass extinction, the largest biocrisis in Earth's history. In this study, analyses of carbonate-associated sulfate (CAS) sulfur, CAS oxygen, and pyrite sulfur-isotope ratios in a continental shelf section from the southern Neo-Tethys Ocean (Spiti Valley, India) provide new insights into the Early Triassic marine sulfur cycle. Secular variation in CAS sulfur-isotope values at Spiti is similar to that in South

China, suggesting that CAS was a robust recorder of a global seawater sulfate signal. The Spiti CAS and pyrite δ^{34} S profiles show that the highest rates of pyrite burial coincided with cooler sea-surface temperatures. We infer that climatic cooling steepened equator-to-pole temperature gradients, invigorating thermohaline overturning circulation, and enhancing upwelling of nutrients that stimulated marine productivity and organic carbon sinking fluxes. Enhanced productivity fueled and sustained microbial respiration, increased oxygen demand, and, within the southern Neo-Tethys, caused the zone of microbial sulfate reduction to migrate upwards and become more connected to the water column. Microbial sulfate reduction, under these conditions, was no longer limited by organic matter or sulfate availability, leading to burial of more ³⁴S-depleted pyrite and ³⁴S- and ¹⁸O-enrichment of the oceanic sulfate pool. This environmental scenario suggests possible environmental stresses related to eutrophication during positive carbon-isotope excursions around the Griesbachian-Dienerian, Dienerian-Smithian, and Smithian-Spathian boundaries. Additionally, the difference between CAS and pyrite sulfurisotope values, $\Delta^{34}S_{CAS-pvr}$, slowly rose through the Early Triassic, reflecting a slow increase in seawater sulfate concentrations following a minimum close to the Permian-Triassic boundary.

Keywords: microbial sulfate reduction; sulfur isotopes; carbonate-associated sulfate; pyrite; Spiti Valley; Neo-Tethys Ocean

1. Introduction

The Permian-Triassic (P-Tr) boundary mass extinction at \sim 252 Ma was the largest biocrisis in Earth's history, during which \sim 90% of marine species and \sim 70% of terrestrial species died out (Erwin, 1994). The marine extinction event lasted \sim 60 kyr (Burgess et al., 2014) and was

linked to environmental changes triggered by eruption of the Siberian Traps Large Igneous Province and the release of massive volumes of greenhouse gases (Renne et al., 1995; Reichow et al., 2009; Svensen et al., 2009; Sobolev et al., 2011; Burgess and Bowring, 2015; Burgess et al., 2017). In contrast to the relatively rapid extinction interval, the Early Triassic recovery was a prolonged multi-step process that was not completed for at least five million years after the end-Permian extinction (Chen and Benton, 2012). Early Triassic ocean temperatures were variable but extremely hot compared to pre-extinction conditions (Joachimski et al., 2012; Sun et al., 2012; Romano et al., 2013; Schobben et al., 2014). Repeated environmental events associated with extreme warming, continental weathering, oceanic stagnation, and marine anoxia likely contributed to the prolonged nature of the Early Triassic recovery (e.g., Wei et al., 2015b). The exact sequence of environmental events during the recovery interval is still being deciphered.

Analysis of changes in the marine biogeochemical sulfur cycle can provide valuable insights into the Early Triassic recovery interval. The sulfur cycle played a major role in shaping marine and terrestrial environmental conditions during the Early Triassic in view of its centrality to volcanic, continental weathering, and marine redox processes (e.g., Wignall, 2001; Wei et al., 2015b). The existing Early Triassic seawater sulfur isotope curve is based mainly on compilations of low-resolution evaporite data (Holser, 1977; Claypool et al., 1980; Cortecci et al., 1981; Worden et al., 1997; Insalaco et al., 2006; Horacek et al., 2010; Bernasconi et al., 2017), and these records reveal only a first-order increase in δ^{34} S values from the P-Tr boundary (ca. +10 %) to a Smithian maximum (ca. +32 %). Apart from the evaporite work, there have been relatively few sulfur isotope studies of Lower Triassic sections to date, limiting our knowledge of high-resolution variation in seawater sulfate δ^{34} S during the Early Triassic (Newton et al., 2004; Riccardi et al., 2006; Gorjan et al., 2007; Marenco et al., 2008; Song-HY et

al., 2014; Schobben et al., 2015; Zhang et al., 2015; Schobben et al., 2017). A δ^{34} S_{CAS}profile for the entire Lower Triassic in the Dajiang and Guandao carbonate platform sections of the eastern Paleo-Tethys (South China) documented major fluctuations at the substage scale, with significant covariation between $\delta^{34}S_{CAS}$ and $\delta^{13}C_{carb}$ (Song-HY et al., 2014). However, the South China $\delta^{34}S_{CAS}$ dataset is marked by large sample-to-sample variability, and its $\delta^{34}S_{CAS}$ values are $\delta^{34}S_{CAS}$ enriched compared to the coeval Early Triassic evaporite record (Bernasconi et al., 2017). Furthermore, the Smithian-Spathian boundary was not analyzed in the Song-HY et al. (2014) study due to a change in lithology from limestone to shale. A study of the Smithian-Spathian boundary in the Shitouzhai section of South China revealed a concurrent decrease in $\delta^{34}S_{CAS}$ and increase in $\delta^{13}C_{carb}$, yielding an inverse relationship that was attributed to strong local upwelling (Zhang et al., 2015). $\delta^{34}S_{CAS}$ data for portions of the Spathian substage were generated at multiple sections in the western United States, yielding δ^{34} S values higher than those in coeval evaporite records (Marenco et al., 2008). To better understand the Early Triassic sulfur cycle and its links to coeval carbon-cycle perturbations and marine environmental changes, additional high-resolution studies of carbonate-associated sulfur and pyrite δ^{34} S are needed.

In this study, we analyze the sulfur isotope compositions of carbonate-associated sulfate (CAS) and pyrite from a southern Neo-Tethyan continental shelf section (Spiti Valley, India) in order to explore variations in the Early Triassic (Griesbachian to earliest Spathian) sulfur cycle. We compare the $\delta^{34}S_{CAS}$ profile for Spiti with $\delta^{34}S_{CAS}$ records for the eastern Paleo-Tethys (South China) in order to evaluate whether these two regions record a common global seawater sulfate signal. Furthermore, through analysis of covariation patterns of $\delta^{34}S_{CAS}$ with $\delta^{34}S_{pyr}$ and $\delta^{18}O_{CAS}$, we identify local and global controls on the Early Triassic marine sulfur cycle.

2. The marine sulfur cycle

The marine biogeochemical sulfur cycle provides an important link to the carbon, oxygen, and iron cycles through microbial sulfate reduction (MSR) and pyrite formation. Relative to the seawater sulfate pool, the marine sulfur cycle major input is from riverine sources influenced by continental weathering and volcanism, and outputs are pyrite and evaporite burial (Bottrell and Newton, 2006). Pyrite forms from the hydrogen sulfide product of MSR. MSR occurs beneath the oxic-anoxic boundary within the water column or sediments. During MSR, sulfate is utilized as an electron acceptor and organic matter is remineralized producing hydrogen sulfide. In the modern ocean, a large proportion of the global MSR flux occurs on the continental shelf (< 200 m in depth), decreases with increasing water-column depth, and generally mimics primary productivity and availability of labile organic matter (Jorgensen, 1982; Canfield, 1991; Bowles et al., 2014). Moreover, in modern continental shelf settings, only 5-20% of the total sulfide formed by MSR is buried as pyrite due to sulfide oxidation and reactive iron availability (Jorgensen, 1982).

MSR isotopically fractionates sulfur between the sulfate pool ($\delta^{34}S_{SO4}$) and resulting sulfide pool, as the lighter ^{32}S isotope is preferentially reduced over the heavier ^{34}S isotope. This can result in differences greater than 60 ‰ between the sulfate and sulfide pools (Rudnicki et al., 2001; Wortmann et al., 2001; Sim et al., 2011). Pyrite retains the isotopic composition of the local sulfide pool from which it forms (Butler et al., 2004). Unlike pyrite $\delta^{34}S$, the $\delta^{34}S$ and $\delta^{18}O$ of CAS can record the isotopic composition of contemporaneous global seawater sulfate owing to the long residence time of sulfate in seawater. $\delta^{18}O_{SO4}$ also fractionates during MSR in the same direction as $\delta^{34}S_{SO4}$ (Mizutani and Rafter, 1969; Mizutani and Rafter, 1973). However, unlike sulfur isotopes, oxygen-isotope exchange occurs between ambient seawater and sulfite

during intermediate steps of MSR (Fritz et al., 1989; Brunner et al., 2005). This process also results in 18 O-enrichment of the sulfate pool by ~29 ‰ if sulfite is reoxidized back to the sulfate pool (Fritz et al. 1989; Wortmann et al., 2007). Furthermore, "direct oxidation" of sulfide (e.g., Markovic et al., 2016), either abiotically or biotically, imparts a distinct and much smaller (~0 to 8 ‰) isotope enrichment (e.g., Balci et al., 2007; Balci et al., 2012) compared to those associated with microbial processes such as oxygen-isotope exchange, MSR, and disproportionation (~8 to 29 ‰) (e.g., Böttcher et al., 2001; Böttcher et al., 2005; Wortmann et al., 2007). In paleomarine studies, it can be difficult to differentiate the importance of MSR, sulfur disproportionation, and sulfide oxidation mechanisms, but tandem analysis of δ^{34} S_{SO4} and δ^{18} O_{SO4} facilitates recognition of changes to the sulfur cycle over time (e.g., Markovic et al., 2015, 2016). This is particularly true if the recorded trends in δ^{34} S_{SO4} and δ^{18} O_{SO4} diverge as, for example, during the end-Permian (Schobben et al., 2015), Cretaceous (Turchyn et al., 2009), and Cenozoic (Turchyn and Schrag, 2006), as well as in modern environments (Mills et al., 2016).

Trace amounts of sulfate that substitute into the carbonate mineral lattice during formation are termed "carbonate-associated sulfate" (CAS) (Takano, 1985; Burdett et al., 1989; Kampschulte and Strauss, 1998; Kampschulte et al., 2001; Kampschulte and Strauss, 2004). The isotope signals of CAS in modern carbonates, both sulfur ($\delta^{34}S_{CAS}$) and oxygen ($\delta^{18}O_{CAS}$), have been shown to reliably record ambient seawater $\delta^{34}S_{SO4}$ and $\delta^{18}O_{SO4}$ (Cortecci and Longinelli, 1971; Kampschulte and Strauss, 1998; Lyons et al., 2004). Whole-rock $\delta^{34}S_{CAS}$, and presumably $\delta^{18}O_{CAS}$, preserve the isotopic composition of coeval seawater by buffering against diagenetic contributions to the whole-rock signal (Lyons et al., 2004; Gill et al., 2008; Rennie and Turchyn, 2014), although this is not always the case (Present et al., 2015). Alteration to the original CAS

seawater signal can result in both minor (< 2-4 ‰; Marenco et al., 2013; Rennie and Turchyn, 2014) and large variations (> 10 ‰; Present et al., 2015) in stratigraphic successions.

3. Study sections and timescale

We analyzed three sections, Mud, Lingti, and Guling, from the Spiti Valley of Himachal Pradesh, India to reconstruct marine conditions at Southern Hemisphere mid-latitudes during the Early Triassic (Fig. 1). Deposition of Spiti Valley sediments occurred at estimated water depths of 50-70 m on a wide continental shelf with a gentle slope along the northern Gondwanan margin of the Neo-Tethys Ocean (Krystyn et al., 2007a; Krystyn et al., 2007b). The majority of samples are from the Mud section, which is a candidate for the GSSP for the Induan-Olenekian (Dienerian-Smithian) boundary (Krystyn et al., 2007a). At Mud, the Lower Triassic Mikin Formation consists of three members: (1) the Lower Limestone Member, (2) the Limestone and Shale Member, and (3) the Niti Limestone Member (Fig. 1C; Bhargava et al., 2004; Krystyn et al., 2007a; Brühwiler et al., 2010b). Although most of the Changsingian substage (uppermost Permian) is missing owing to a depositional hiatus, the occurrence of the ammonoid Cyclolobus suggests at least the early Changhsingian, if not more, is present (e.g., Bhargava, 2008). The Griesbachian (lowermost Triassic) is stratigraphically complete or nearly so based on the presence of the conodont fossil Hindeodus parvus at the base of the Lower Limestone Member (Orchard and Krystyn, 1998; Krystyn et al., 2004). The Lower Limestone Member corresponds to the Griesbachian and lowermost Dienerian, and the overlying Limestone and Shale Member spans the remainder of the Dienerian and the entire Smithian. The latter member consists of alternating shale and limestone beds and contains the Ambites, Flemingites, and

Parahedenstroemia Beds. The base of the Niti Limestone Member is within the lower Spathian (Bhargava et al., 2004; Krystyn et al., 2007a).

The Lingti and Guling sections were compared to Mud's stratigraphy to create a composite Spiti Valley section. The biostratigraphy of the Mud section is well established based on ammonoid (Bhargava et al., 2004; Krystyn et al., 2004; Krystyn et al., 2007a; Brühwiler et al., 2010a; Brühwiler et al., 2010b; Brühwiler et al., 2012; Ware et al., 2015) and conodont studies (Orchard and Krystyn, 1998; Krystyn et al., 2004; Krystyn et al., 2007a; Goudemand, 2014). The Griesbachian substage is defined by the Otoceras ammonoid Zone in all three sections (Orchard and Krystyn, 1998; Krystyn et al., 2004). Other biozones have not been identified at Lingti so the stratigraphic divisions were based on proportional thicknesses of the *Otoceras* Zone at Lingti compared to Mud. For Guling, the length of the *Pluerogyronties planidorsatus* ammonoid Zone was compared with that at Mud (Krystyn et al., 2004; Krystyn et al., 2007a; Fig. 2; Fig. 3). At Mud, the conodont-based Induan-Olenekian (Dienerian-Smithian) boundary was placed within the Flemingites Beds (~4.6 m; Krystyn et al., 2007a, b) while the ammonoid-based boundary was placed about one meter lower in the *Ambites* Beds (~3.8 m; Brühwiler et al., 2010b). Using both fossil-based boundaries in combination with the carbon-isotope profile, we use a value of 4.2 m for dividing samples between the Dienerian and Smithian substages. The fossil-based Smithian-Spathian boundary was placed at around 15 m (Krystyn et al., 2007a). We use a value of 13.8 m based on the carbon-isotope profile and the newly proposed definition by Zhang et al. (in review) for the Smithian-Spathian boundary. The majority of samples were from the Mud section with a few samples from Guling (n = 4) and Lingti (n = 7) to fill in sample gaps throughout the Griesbachian and Dienerian.

We adopted the Early Triassic timescale of Algeo et al. (2013) and Shen et al. (2015), adjusted for the new Burgess et al. (2014) age of the P-Tr boundary. The key boundary ages include: P-Tr boundary (251.9 Ma), Griesbachian-Dienerian boundary (251.3 Ma), Dienerian-Smithian boundary (251.0 Ma), Smithian-Spathian boundary (250.6 Ma), and Spathian-Anisian boundary (247.2 Ma). These age tie-points permitted construction of an age-depth model for the composite Spiti section (Fig. S4; note "S" indicates material in the Supplemental File). Sedimentation rates at Spiti ranged from 1.1 m Myr⁻¹ to 24.0 m Myr⁻¹, with peak rates during the Smithian (Fig. S4).

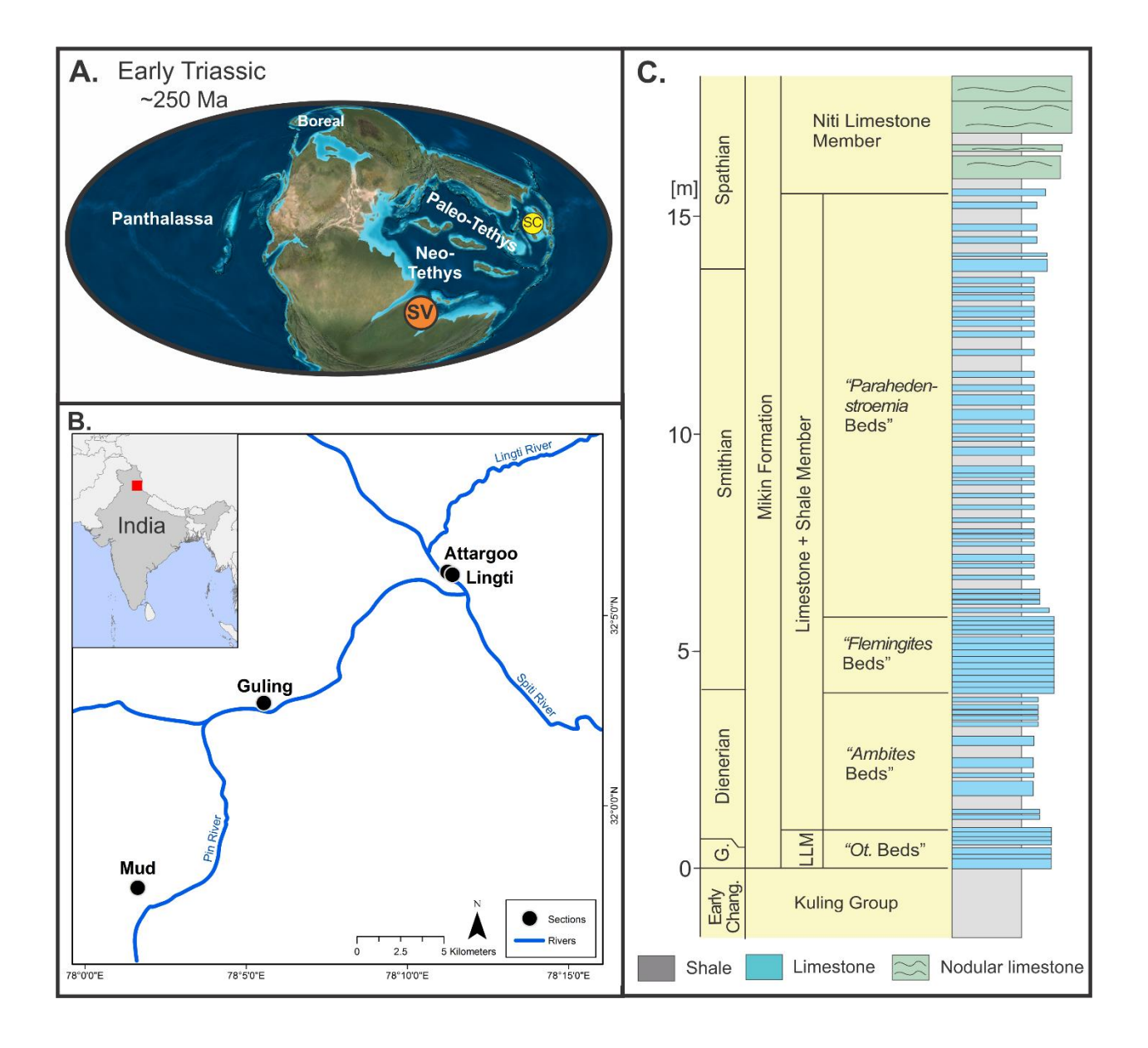


Figure 1. (A) Early Triassic paleogeography (modified from Colorado Plateau Geosystems image, updated by Ron Blakey, 2018). Shown are the paleolocations of the Spiti Valley study sections (orange; SV) within the southern Neo-Tethys, and the South China sections (yellow; SC) within the eastern Paleo-Tethys. (B) Locations of the study sections (circles) within the Spiti Valley. We analyzed the Mud, Lingti, and Guling sections in this study. Panel made using the ArcGIS program and databases. (C) Generalized lithological diagram of the Mud section (modified from Brühwiler et al., 2010b). Abbreviations: Chang. – Changhsingian, G. – Griesbachian, LLM – Lower Limestone Member, Ot. – *Otoceras*.

4. Methods

We used previously published elemental concentration data for most Mud samples (Wei et al., 2015b). For new samples, we performed all analyses at the School for the Environment's Environmental Analytical Facility (EAF) at the University of Massachusetts Boston, unless otherwise noted.

4.1. CAS extraction

We extracted 75 Spiti Valley carbonate samples for CAS. The CAS extraction method for this study follows the recommendation of Wotte et al. (2012). Briefly, we leached powdered samples with 10 % NaCl for 24-hour intervals to remove any NaCl-soluble sulfur. We repeated this step until no further precipitation of BaSO₄. After removal of all soluble sulfur, we dissolved carbonate in 25 % HCl to release carbonate bound sulfate into solution. We added 10 % BaCl₂ solution to precipitate the released CAS as BaSO₄. We filtered, dried, and weighed the precipitate to stoichiometrically calculate CAS concentration as SO₄²⁻. We dried and collected the HCl insoluble residue for pyrite extraction. For two samples (AL2-16/19 and AL2-21/25), we combined two stratigraphically distinct samples to obtain sufficient material for CAS extraction. The ranges of these combined samples do not overlap with any other samples.

4.2. Pyrite extraction

On the insoluble residue following the CAS extraction, we extracted pyrite from all samples and a subset of whole-rock samples to compare values (Section S1). The extraction procedure and setup followed a modified chromium reduction method (Canfield et al., 1986; Sullivan et al.,

2000). We gently boiled the reaction for one hour under continuous N_2 flow, releasing pyrite as H_2S gas. A zinc acetate trapping solution, trapped the H_2S gas as ZnS. By adding silver nitrate, we converted the ZnS to Ag_2S . We filtered, dried, and weighed the Ag_2S to stoichiometrically calculate pyrite sulfur concentrations (S_{pyr}) . Calculated S_{pyr} values for the CAS residues were carbonate corrected to adjust for the material dissolved during CAS extraction and provide an estimate of whole-rock concentrations.

4.3. Sulfur and oxygen isotope measurements

For sulfur-isotope analyses ($\delta^{34}S_{CAS}$ and $\delta^{34}S_{DVI}$), we weighed 0.3-0.4 mg of BaSO₄ (for $\delta^{34}S_{CAS}$) or Ag₂S (for $\delta^{34}S_{pvr}$) into tin capsules with vanadium pentoxide to aid in combustion. We measured the sulfur-isotope ratios on a Costech Elemental Analyzer ECS 4010 connected to a Thermo Delta V+ Isotope Ratio Mass Spectrometer. We expressed the isotope ratios in per mille notation (‰) relative to Vienna Canyon Diablo Troilite (VCDT). To calibrate $\delta^{34}S$ values, we used three IAEA silver sulfide standards, IAEA-S-1 (-0.3 %), IAEA-S-2 (+22.67 %), and IAEA-S-3 (-32.55 %), and a check standard, NBS-127 (+21.1 %). Precision was less than 0.35 ‰ (1σ) based on replicate measurements of the three IAEA calibration standards and was corrected for population size (>3 measurements per standard per run). $\Delta^{34}S_{CAS-pyr}$ values are the difference between paired $\delta^{34}S_{CAS}$ and $\delta^{34}S_{DVI}$ values. For oxygen-isotope measurements of CAS $(\delta^{18}O_{CAS})$, we weighed 0.3-0.4 mg of BaSO₄ into silver capsules and measured isotope values on a TC/EA connected to a Thermo Delta V+ Isotope Ratio Mass Spectrometer. We expressed the isotope ratios in per mille notation relative to Vienna Standard Mean Ocean Water (VSMOW). To calibrate $\delta^{18}O$ values, two IAEA barium sulfate standards, IAEA-SO-5 (+12.13 %) and IAEA-SO-6 (-11.35 %), and a check standard, NBS-127 (+8.59 %), were used. Precision was

less than $0.55 \% (1\sigma)$ based on replicate measurements of the two IAEA standards and was corrected for population size (>4 measurements per standard per run).

4.4. Pyrite morphology

Using a JEOL JSM-6010LA IntouchScope Scanning Electron Microscope, we examined pyrite morphology. Polished whole-rock chips were gold coated and observed in back-scatter electron mode. For the six samples between 4.63 to 5.63 m of Mud, we observed pyrite morphology on the CAS residue since no whole-rock remained for this interval. We estimated the relative abundance of framboidal and euhedral pyrite for each sample. When pyrite framboids were common, we measured the diameter of pyrite framboids using the built-in measuring tools on the Intouch Scope program. We used energy dispersive spectrometry to determine if there was any significant S_{pyr} loss due to modern oxidative weathering.

4.5. $\delta^{13}C_{carb}$ and $\delta^{18}O_{carb}$ measurements

The majority of Spiti Valley samples (93 out of 115) were measured for $\delta^{13}C_{carb}$ and $\delta^{18}O_{carb}$ at the University of Kentucky Environmental Research Training Laboratory using a GasBench II peripheral coupled to a DeltaPlusXP Isotope Ratio Mass Spectrometer (IRMS). Samples $(450\pm50~\mu g)$ were equilibrated at 40 °C for 24 h before analysis. Average precisions (1σ) were 0.05~% for $\delta^{13}C$ and 0.05~% for $\delta^{18}O$ of the NBS-19 standard $(\delta^{13}C:+1.95~\%; \delta^{18}O:-2.20~\%)$, and 0.02~% for $\delta^{13}C$ and 0.05~% for $\delta^{18}O$ of unknowns. We measured the remaining subset of carbonate samples (22 out of 115) for $\delta^{13}C_{carb}$ values on a Thermo Scientific GasBench II coupled to a Thermo Delta V+ IRMS at the University of Massachusetts Boston. For each sample and standard, we measured $500\text{-}600~\mu g}$ into a 12 mL borosilicate round bottom vial

capped with a butyl rubber septum. We flushed the vials with helium and digested the sample with 85 % phosphoric acid at 25 °C for 12 hours before isotope measurement. We used the NBS-19 (\pm 1.95 %) and IA-R022 (\pm 28.63 %) standards to calibrate the measured values, and we expressed the isotope ratios in per mille notation relative to Vienna Pee Dee Belemnite (VPDB). Precision was better than \pm 0.2 % based on replicate measurements of the standards.

4.6. Major-element concentrations

We used elemental concentrations determined by Wei et al. (2015b) for the majority of carbonate samples at Spiti Valley (93 out of 115). Using a Spectro XEPOS Bench Top Energy Dispersion X-ray Fluorescence, we measured elemental concentrations (Al, Ca, Mg, Mn, and Sr) for the subset of samples (22 out of 115) not analyzed in Wei et al. (2015b). We filled capsules with powdered sample and measured each sample in triplicate under He purge. We repeatedly measured USGS SDO-1, NIST 1d, and NIST 88b standards to produce a linear three-point calibration curve for each element. For a check standard, we repeatedly measured the USGS standard SGR-1b as an unknown sample. Check standard results were generally within 10 percent difference of certified values. In this study, we used the whole-rock Mn/Sr values as a proxy of the Mn/Sr ratios of the carbonate lattice. This is suitable due to the generally very low amount of detrital Mn and Sr (see Zhang et al., 2015, for an example). However, for Ca/(Ca+Mg) ratios, we used the upper continental crust element concentration per unit of Al (McLennan, 2001) to estimate the non-detrital ratio.

5. Results

5.1. Carbon and sulfur isotopes

All isotope ratios varied significantly throughout the Lower Triassic at Spiti Valley (see Fig. 2 for a depth scale, see Fig. 3 for an age scale; further references are to Fig. 3). The $\delta^{13}C_{carb}$ profile matches the pattern associated with the Early Triassic globally (Payne et al., 2004; Horacek et al., 2007a; Horacek et al., 2007b; Horacek et al., 2009; Song-HY et al., 2013). The $\delta^{13}C_{carb}$ profiles for Lingti and Guling conform to the more-detailed profile for Mud, providing confidence in the composite section (Fig. 3). $\delta^{13}C_{carb}$ values peaked around the Griesbachian-Dienerian boundary, Dienerian-Smithian boundary, and Smithian-Spathian boundary, with minima in the lower Griesbachian, Dienerian, and middle to upper Smithian (Fig. 3A). There is no statistically significant correlation (Spearman's rho; r_s) between $\delta^{13}C_{carb}$ and $\delta^{18}O_{carb}$ (r_s = -0.17, p-value = 0.10) or $\delta^{18}O_{carb}$ and $\delta^{34}S_{CAS}$ (r_s = -0.02, p-value >0.10).

 $\delta^{34} S_{CAS}$ ranges from +8.3 to +36.3 ‰ with an average of +27.5 ‰ (Fig. 3B). $\delta^{34} S_{CAS}$ increased through the Griesbachian from about +10 to +23 ‰. A change in slope occurred around the Griesbachian-Dienerian boundary, as $\delta^{34} S_{CAS}$ remained at ca. +21 ‰ through the mid-Dienerian. Values began to increase again to a lowermost Smithian maximum of ca. +36 ‰. The values then decreased to ca. +30 ‰ in the upper Smithian before increasing sharply at the Smithian-Spathian boundary. $\delta^{18} O_{CAS}$ ranges from +9.7 to +24.7 ‰ with an average of +17.2 ‰. $\delta^{18} O_{CAS}$ generally followed the same trends as $\delta^{34} S_{CAS}$ (Fig. 3C), and they are significantly correlated (r_s = +0.51; p-value < 0.001; Fig. 3F). However, $\delta^{18} O_{CAS}$ contained a smaller range of values that was less sensitive to change, for instance, during a $\delta^{34} S_{CAS}$ shift from +23 to +36 ‰ around the Dienerian-Smithian boundary, the corresponding change in $\delta^{18} O_{CAS}$ was only from +14 to +18 ‰.

There is no statistical difference between $\delta^{34}S_{pyr}$ values extracted from whole-rock samples and CAS residues (Section S1). However, S_{pyr} values calculated from the CAS residues were

relatively lower and showed reduced variation compared to the whole-rock values (Section S1). Nevertheless, the S_{pyr} values from CAS residues are robust and match trends seen in the whole-rock values. Further discussion of $\delta^{34}S_{pyr}$ and S_{pyr} refers to the values measured from the CAS residues. $\delta^{34}S_{pyr}$ ranges from -21.4 % to +22.9 % with an average of -2.0 %. The $\delta^{34}S_{pyr}$ profile exhibits relative minima of ca. -15 % in the lower Griesbachian, middle Dienerian, lower Smithian, and lower Spathian (Fig. 3D). $\delta^{34}S_{pyr}$ values scattered widely with a mean of ca. 0 % through most of the middle Smithian. The $\Delta^{34}S_{CAS-pyr}$ values range from +4.1 % to +54.8 % with an average of +29.5 %. $\Delta^{34}S_{CAS-pyr}$ maxima are present in the upper Griesbachian, lower Smithian, and lower Spathian (Fig. 3E). There was a broadly decreasing trend through the Dienerian to a relative minimum in the lowermost Smithian. The middle Smithian varied largely around +30 % before increasing in the upper Smithian to lower Spathian (Fig. 3E).

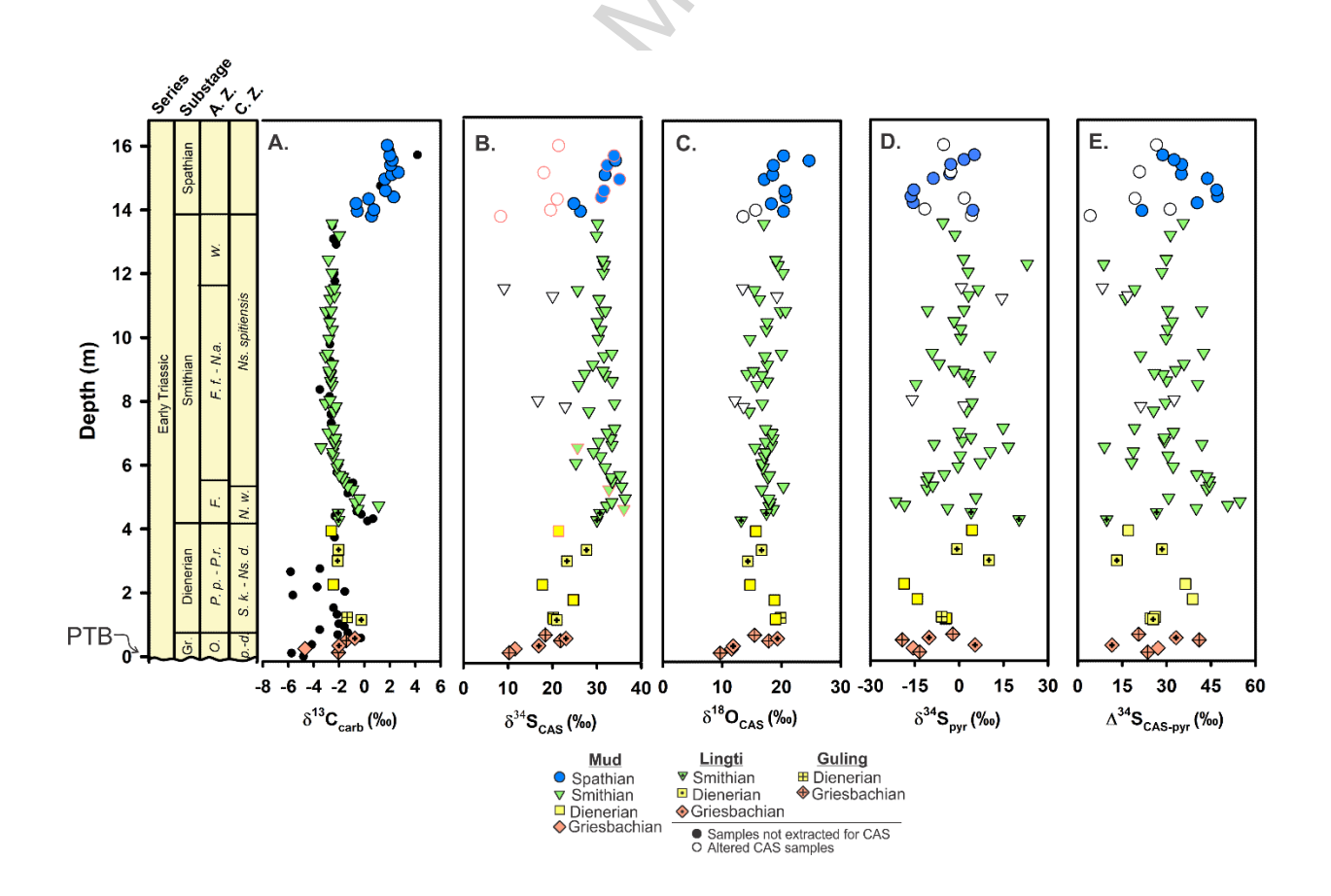


Figure 2: Composite stratigraphic profiles for Spiti Valley carbon and sulfur isotopes. The Permian-Triassic Boundary (PTB) may be missing due to a depositional hiatus (wavy line; Bhargava, 2008), but the Griesbachian is regarded as nearly complete owing to the presence of *Hindeodus parvus* near its base (Orchard and Krystyn, 1998; Krystyn et al., 2004). (A) δ¹³C_{carb} (B) δ³⁴S_{CAS} with the red outlines marking Mn/Sr greater than 6. (C) δ¹⁸O_{CAS} (D) δ³⁴S_{pyr} (E) Δ³⁴S_{CAS-pyr} (i.e., δ³⁴S_{CAS} – δ³⁴S_{pyr}). Note: some samples were analyzed for C isotopes but not S isotopes, and CAS samples deemed altered were designated with white markers (Section 6.1). Abbreviations: A. Z. – Ammonoid Zones, C. Z. – Conodont Zone, O. – Otoceras woodwardi to Ophiceras tibeticum; P. p. – Pleurogyronites planidorsatus; P.r. – Prionolobus rotundatus; F. – Flemingites bhargavai to Rohillites rohilla; F.f. - Flemingites flemingianus; N. a. - Nyalamites angustecostatus; W. – Wasatchites distractus to Glytophiceras sinuatum;; p. – Hindeodus parvus; d. – Neoclarkina discreta; S.k. – Sweetspathodus kummeli; Ns. – Neospathodus; d. – dieneri; N.w. – Novispathodus waageni; Gr. – Griesbachian; and PTB – Permian-Triassic Boundary. Note, potential analytical error is associated with measured δ¹⁸O values above +12.13 % and δ³⁴S values above +22.67 as isotope calibration standards did not cover the upper limit of measured values for Spiti Valley samples.

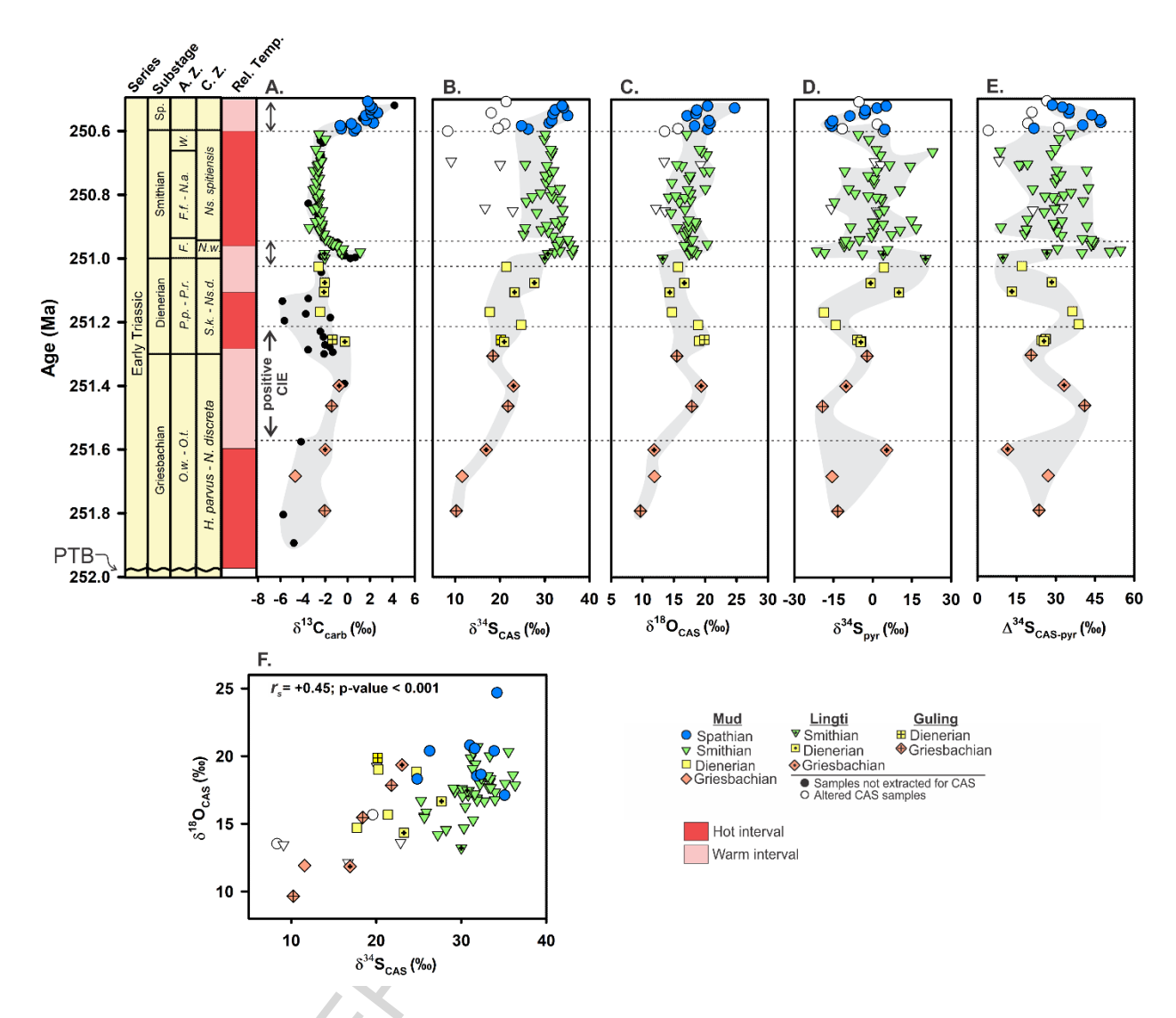


Figure 3. Composite trends for Spiti Valley carbon and sulfur isotopes. The figure is similar to Figure 2 but vertical scale is based on age defined by the age-depth model (Fig. S4). The Permian-Triassic Boundary (PTB) may be missing due to a depositional hiatus (wavy line; Bhargava, 2008), but the Griesbachian is regarded as nearly complete owing to the presence of *Hindeodus parvus* near its base (Orchard and Krystyn, 1998; Krystyn et al., 2004). (A) $\delta^{13}C_{carb}$; (B) $\delta^{34}S_{CAS}$; (C) $\delta^{18}O_{CAS}$; (D) $\delta^{34}S_{pyr}$; (E) $\Delta^{34}S_{CAS-pyr}$ (i.e., $\delta^{34}S_{CAS} - \delta^{34}S_{pyr}$); (F) $\delta^{34}S_{CAS}$ vs. $\delta^{18}O_{CAS}$. Note: some samples were analyzed for C isotopes but not S isotopes, and CAS samples deemed altered were designated with white markers (Section 6.1). The gray bands show overall secular trends. 'Hot' and 'warm' (i.e., less hot) intervals based on conodont $\delta^{18}O$ records from South China (Joachimski et al., 2012; Sun et al., 2012) and Pakistan (Romano et al., 2013). Abbreviations: Rel. Temp. – Relative Temperature, *O.w. – Otoceras woodwardi; O.t. – Ophiceras tibeticum; H. – Hindeodus; N. - Neoclarkina*; and Sp. – Spathian. Further abbreviations listed in Figure 2. Note, potential analytical error is associated with measured $\delta^{18}O$ values above +12.13 % and $\delta^{34}S$ values above +22.67 as isotope calibration standards did not cover the upper limit of measured values for Spiti Valley samples.

5.2. Pyrite sulfur and elemental concentrations

 S_{pvr} ranges from 0.01 % to 0.47 % with an average of 0.08 % but shows no systematic relationship to δ^{34} S_{CAS} values ($r_s = -0.007$, p-value > 0.10). Higher values are observed in the Smithian and Spathian (Fig. 4A). S_{pyr} concentrations covary negatively with $\delta^{34}S_{pyr}$ values ($r_s = -$ 0.54, p-value < 0.001; Fig. 4C). Evidence for partial S_{pvr} loss due to modern oxidative weathering is present in some Griesbachian and Dienerian samples (Fig. 4A; Section S2). Framboidal pyrite was rare or absent in most samples, and euhedral pyrite was the most common form throughout the study section. Framboidal pyrite was relatively more abundant in the Griesbachian to lower Dienerian and uppermost Smithian than within other intervals (Fig. 4B). Where framboidal pyrite is more common (n > 30), the mean framboid diameters range from 7.8 to 13.4 µm with an average of 10.2 µm (Fig. 4D). Petrographic observation revealed both unaltered and infilled framboidal crystal habits (Fig. 5). Al values for CAS-extracted samples range from 0.04 % to 5.4 % with an average of 1.9 % but show no systematic relationship to δ^{34} S_{CAS} values ($r_s = -0.02$, p-value >0.10; Table S3). Non-detrital molar ratios of Ca/(Ca+Mg) are close to 1.0 for most CAS-extracted samples (mean = 0.98) and show no systematic relationship to δ^{34} S_{CAS}($r_s = +0.10$, p-value >0.10; Table S3). Mn values range from 36 to 6493 ppm with an average of 1280 ppm, and Sr values range from 171 to 1165 with an average of 339. The ratios of Mn/Sr for CAS-extracted samples range from 0.04 to 18.3 with an average of 4.5. There is no significant relationship between Mn/Sr and δ^{34} S_{CAS} values ($r_s = +0.06$, p-value >0.10; Fig. 6A), or between Mn/Sr and $\delta^{18}O_{CAS}$ values ($r_s = +0.09$, p-value >0.10; Fig. 6B). However, there are significant correlations between Mn/Sr and δ^{34} S_{pyr}values ($r_s = -0.28$, p-value = 0.02; Fig. 6C), and between Mn/Sr and δ^{13} C_{carb} values ($r_s = +0.34$, p-value < 0.001; Fig. 6D).

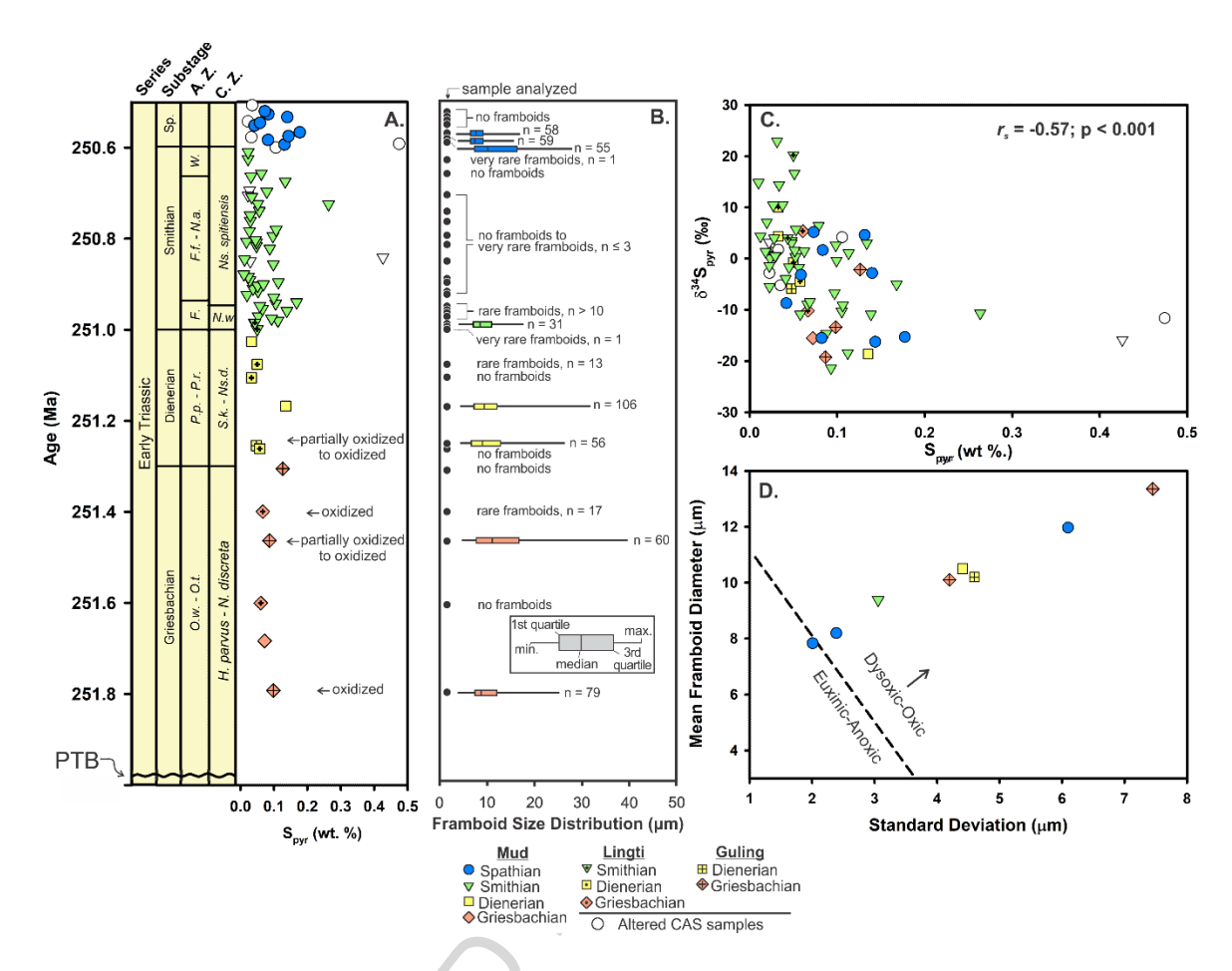


Figure 4. (A) Secular S_{pyr} variation. (B) Box-and-whisker plots of framboid size distributions for samples that contain more than 30 measured pyrite framboids. Other samples contain no framboids (n = 0), very rare framboids (n \leq 3), or rare framboids (n \leq 30). (C) $\delta^{34}S_{pyr}$ vs S_{pyr} values. The correlation coefficient (r_s = -0.57, p-value \leq 0.001) does not include the altered CAS samples (white markers; Section 6.1). The negative relationship is consistent with mixing of isotopically heavy diagenetic pyrite and isotopically light syngenetic (framboidal) pyrite (cf. Algeo et al., 2008; Wei et al., 2015a; Shen et al., 2016). (D) Mean framboid diameter vs standard deviation for samples with 30 or more pyrite framboids. The dashed line marks the boundary between euxinic-anoxic and dysoxic-oxic redox zones (Wilkin et al., 1996; Bond and Wignall, 2010). Abbreviations are listed in Figures 2 and 3.

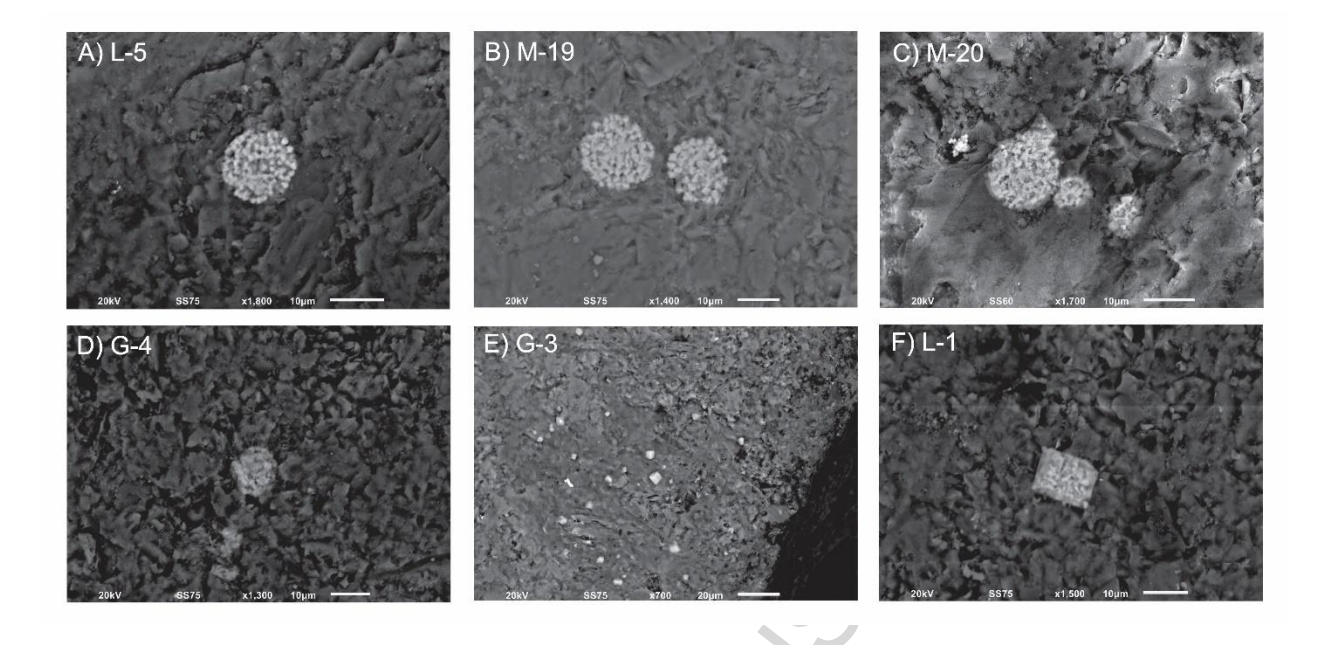


Figure 5. Examples of pyrite. (A-B) Framboidal pyrite with individual microcrystals from samples L-5 and M-19, respectively. (C-D) Framboidal pyrite with partial infilling and loss of individual microcrystals from samples M-20 and G-4, respectively. The framboidal crystal form can still be identified and measured. (E-F) Euhedral pyrite crystals in samples G-3 and L-1, respectively.

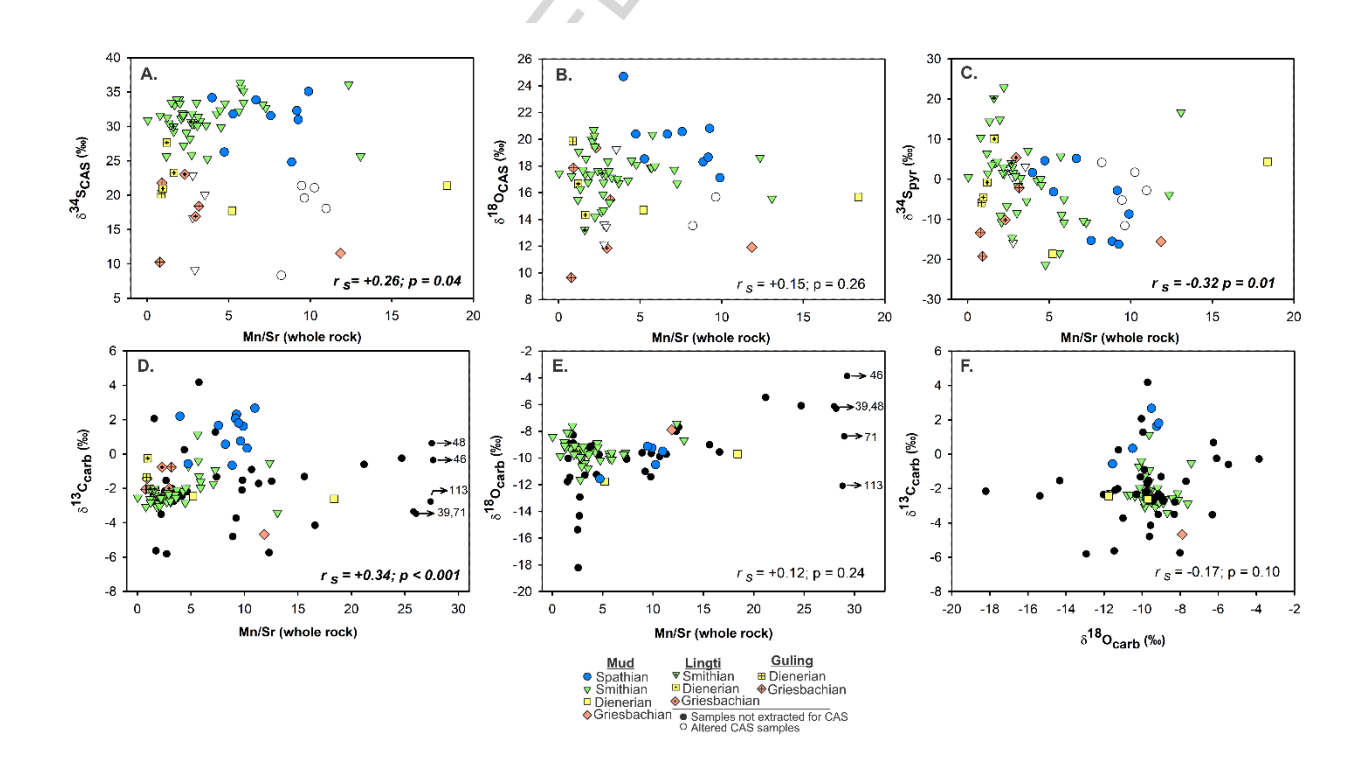


Figure 6. The relation between Mn/Sr ratios and (A) $\delta^{34}S_{CAS}$, (B) $\delta^{18}O_{CAS}$, (C) $\delta^{34}S_{pyr}$, (D) $\delta^{13}C_{carb}$, and (E) $\delta^{18}O_{carb}$, and (F) $\delta^{13}C_{carb}$ vs. $\delta^{18}O_{carb}$, for all study samples. r_s is Spearman's rho correlation coefficient, with significant correlations (p(α) < 0.05 (2 σ)) given in bold. Altered CAS samples (open symbols) are shown in panels A-C (see Section 6.1) but not included in the calculation of r_s . Mud carbonate samples for which CAS was not extracted (black circles) are shown in panels D-F. Note, potential analytical error is associated with measured $\delta^{18}O$ values above +12.13 ‰ and $\delta^{34}S$ values above +22.67 as isotope calibration standards did not cover the upper limit of measured values for Spiti Valley samples.

6. Discussion

6.1. Evaluation of primary origin of CAS signal

Because our overall goal was to reconstruct changes in seawater sulfate composition during the Early Triassic, we evaluated potential alteration of measured CAS-isotope values. Such alteration can result from post-depositional processes (e.g., Present et al., 2015) or pyrite oxidation during the extraction process (e.g., Wotte et al., 2012). To identify potentially altered samples, we flagged any sample where the $\delta^{34}S_{CAS}$ value was more than 10 % different from one of its nearest neighbors (Table S1). This procedure yielded nine samples that are potentially altered from their original seawater sulfate isotope values (AL2-113, AL2-109, AL2-104, M-18, M-17, AL2-87, AL2-85, AL2-64, AL2-62; Table S1). In all 9 cases, the flagged samples exhibit $\delta^{34}S_{CAS}$ values less than those of their nearest neighbors. This pattern suggests that pyrite oxidation during CAS extraction was the likely cause of alteration. Further statistical tests and discussion of isotopic trends do not include these 9 potentially altered samples.

Processes that can alter primary $\delta^{34}S_{CAS}$ and $\delta^{18}O_{CAS}$ values include dolomitization, local microbial sulfate reduction (MSR), detrital influences, and burial diagenesis of the carbonate host rock. For example, dolomitized limestone and dolostones may exhibit systematically lower $\delta^{34}S_{CAS}$ values compared to co-occurring limestones (Marenco, 2007; Marenco et al., 2008). At Spiti Valley, there is little evidence for systematic alteration due to dolomitization based on non-

detrital Ca/(Ca+Mg) ratios that are close to 1.0 and a lack of correlation of Ca/(Ca+Mg) with $\delta^{34}S_{CAS}(r_s = -0.008, p-value > 0.10)$. There is also little evidence for systematic variation due to local MSR based on a lack of correlation between $\delta^{34}S_{CAS}$ and S_{pyr} concentrations ($r_s = -0.03$; p-value > 0.10), or for detrital influences, based on a lack of correlation between $\delta^{34}S_{CAS}$ and Al concentrations ($r_s = +0.12$; p-value > 0.10). Thus, these factors may have contributed to minor sample-to-sample variability in the sulfur and oxygen isotope profiles (Fig. 3), but they are unlikely to have been the dominant controls on long-term secular trends.

Potential diagenetic alteration of original seawater sulfate δ^{34} S or δ^{18} O values in the Spiti Valley samples can be assessed using Mn/Sr ratios. In carbonates, Mn/Sr ratios < 2 (Derry et al., 1992) or < 3 (Kaufman et al., 1993) are considered to represent largely unaltered material. Although some studies have suggested that primary $\delta^{13}C_{carb}$ signatures can be preserved up to Mn/Sr ratios of ~10 (Kaufman and Knoll, 1995), a lower Mn/Sr cutoff (0.5 or less) may be preferable for more easily altered systems like Sr isotopes (Montañez et al. 1996). A large majority of the present study samples yielded Mn/Sr ratios < 6 (n = 52/64) with only four samples > 10, and the relationship between $\delta^{18}O_{CAS}$ and Mn/Sr is not significant ($r_s = +0.15$; Fig. 6B). However, weak to moderate correlations between Mn/Sr and $\delta^{34}S_{CAS}(r_s = +0.26; Fig. 6A)$ and between $\delta^{13}C_{carb}$ and Mn/Sr ($r_s = +0.34$; Fig. 6D) are a concern as they may indicate diagenetic influences. However, several observations argue against major diagenetic effects, i.e., to the extent that the primary marine carbon and sulfur isotope signals have not been preserved. First, the first-order trends in the $\delta^{13}C_{carb}$ profile at Spiti match those of other Lower Triassic sections globally (Horacek et al., 2007a; Horacek et al., 2007b; Horacek et al., 2009; Song-HY et al., 2013). Second, comparison of the $\delta^{34}S_{CAS}$ of samples with high Mn/Sr ratios (> 6) to neighboring samples with lower Mn/Sr ratios reveals no systematic pattern of S-isotopic

enrichment or depletion (Fig. 2), suggesting that these samples may preserve a primary marine CAS-isotope signal despite high Mn/Sr values. Third, the secular pattern of positive and negative shifts in $\delta^{34}S_{CAS}$ through the Lower Triassic at Spiti is similar to those for coeval sections in South China, suggesting that both regions have recorded a common global seawater signal that has not been obscured by diagenetic alteration (see Section 6.2). Thus, we infer that the Spiti Valley sections yield a primary marine $\delta^{34}S$ record despite a modest level of diagenetic alteration of the host carbonate.

6.2. Global trends in $\delta^{34}S_{CAS}$

Although $\delta^{34}S_{CAS}$ has been analyzed in a number of Permian-Triassic boundary sections, it has received scant attention in sections younger than the earliest Griesbachian (Marenco, 2007; Marenco et al., 2008; Song-HY et al., 2014; Zhang et al., 2015). Among those studies, only $\delta^{34}S_{CAS}$ profiles for the eastern Paleo-Tethys sections are sufficiently high-resolution (Song-HY et al., 2014; Zhang et al., 2015) to compare with southern Neo-Tethys profiles of the Spiti Valley to determine possible global trends (Fig. 7). The $\delta^{34}S_{CAS}$ profiles of the eastern Paleo-Tethys and southern Neo-Tethys are similar from the Griesbachian to the Smithian-Spathian boundary, suggesting a common global CAS signal (Fig. 7). During the Griesbachian N1-to-P1 positive CIE (nomenclature from Song-HY et al., 2013), both regions exhibit increasing $\delta^{34}S_{CAS}$ values. Evaporite $\delta^{34}S$ also increased sharply through this interval (ca. +15 ‰ to +25 ‰; Bernasconi et al., 2017). During the P1-to-N2 negative CIE, $\delta^{34}S_{CAS}$ was variable in both Spiti Valley and South China but no secular trends are apparent. The evaporite record also suggests relatively uniform seawater $\delta^{34}S$ during the early to mid-Dienerian (Insalaco et al., 2006; Bernasconi et al., 2017). During the Dienerian to early Smithian N2-to-P2 positive CIE, $\delta^{34}S_{CAS}$ values increased

rapidly again (Fig. 7). This increase began from a minimum of +15-20 ‰ for the Spiti Valley and from +20-25 ‰ for South China and reached maxima of +35-40 ‰ at the end of the CIE for both regions. In contrast, the end-Dienerian maximum in the evaporite δ^{34} S record is ca. +25 ‰ to +30 ‰ (Bernasconi et al., 2017). During the P2-to-N3 negative CIE, δ^{34} S_{CAS} decreased in both regions (from +35 to +30 ‰ at Spiti, and from +35-40 to +20-25 ‰ in South China; Fig. 7), and during the Smithian-Spathian boundary N3-to-P3 positive CIE both regions record rising δ^{34} S_{CAS} values. The evaporite record does not offer sufficient resolution from the Smithian to early Spathian to permit a comparison (Bernasconi et al., 2017). Overall, the secular patterns of δ^{34} S_{CAS} variation in the Spiti Valley and South China were quite similar throughout the Early Triassic.

Despite similar $\delta^{34}S_{CAS}$ trends, there were significant differences in absolute $\delta^{34}S_{CAS}$ values between the Spiti Valley and South China. The largest differences are observed during the Griesbachian and Dienerian, when the range of $\delta^{34}S_{CAS}$ values in the Spiti Valley (ca. +10 to +23 %) was about 10 % lower than that in South China (ca. +20 to +33 %; Fig. 7). These differences are statistically significant, as shown by an independent-samples t-test yielding t(63) = 3.04, p-value = 0.003 for the Griesbachian, and t(46) = 2.63, p-value = 0.012 for the Dienerian. A comparison of $\delta^{34}S$ between the Spiti Valley and the evaporite record (Bernasconi et al., 2017) shows similar absolute values during the Griesbachian (t(15) = -0.70, p-value = 0.50) but statistically different values during the Dienerian (t(12) = 3.97, p-value = 0.001). On this basis, we infer that the CAS record for South China was ^{34}S -enriched during the Griesbachian relative to the global mean (as recorded by Spiti Valley and the evaporite record), but that it nonetheless preserves relative secular trends.

The origin of the observed differences in Lower Triassic $\delta^{34}S_{CAS}$ records is uncertain, and several possible causes can be considered. First, the South China $\delta^{34}S_{CAS}$ record may not faithfully record primary seawater $\delta^{34}S_{904}$ but are ^{34}S -enriched due to some diagenetic process. However, diagenesis did not completely overprint the primary $\delta^{34}S$ signal as the secular trends in the South China and Spiti Valley records are quite similar. Second, regional variation in seawater sulfate isotopic compositions may have existed during the Griesbachian and Dienerian owing to low seawater sulfate concentrations (<3 mM; Luo et al., 2010; Schobben et al., 2017 or 2-6 mM; Bernasconi et al., 2017) and a shortening of the residence time of sulfate in seawater following the P-Tr boundary event (Song-HY et al., 2014). Regional variation in seawater sulfate δ^{34} S may have developed owing to oceanographic factors such as local marine redox conditions or semirestriction of craton-interior seas (e.g., in South China). During the Griesbachian and Dienerian, redox conditions in the southern Neo-Tethys Ocean were mostly oxic or dysoxic (Wei et al., 2015b; Fig. 4D) whereas those in the eastern Paleo-Tethys Ocean were frequently anoxic or euxinic (Song et al., 2012; Tian et al., 2014). Generally more reducing conditions in the South China region would have promoted more intense MSR leading to regionally higher seawater sulfate δ^{34} S values. Significantly, the convergence of the δ^{34} S_{CAS} profiles of the two regions by the early Smithian (independent-samples t-test: t(95) = -1.69, p-value = 0.09) is consistent with a general increase in seawater sulfate concentrations during the Early Triassic (Stebbins et al., in press; with further increases during the Middle Triassic, see Bernasconi et al., 2017), which would have increased the residence time of global seawater sulfate and minimized the potential for regional variations (see Section 6.3.2).

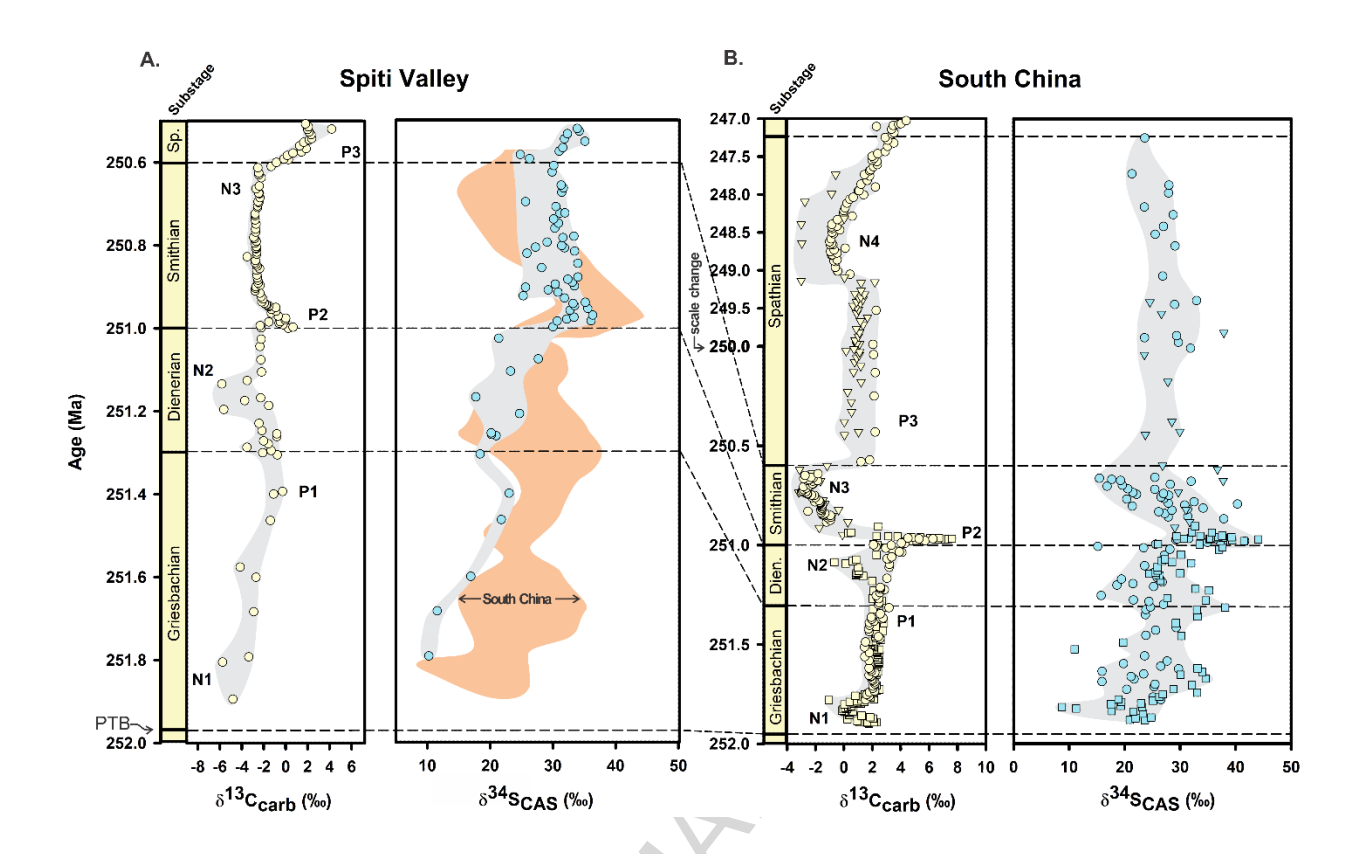


Figure 7. $\delta^{13}C_{carb}$ and $\delta^{34}S_{CAS}$ comparisons between Spiti Valley (this study) and South China (Song-HY et al., 2014; Zhang et al., 2015). Gray bands highlight secular trends. The orange band in the Spiti Valley $\delta^{34}S_{CAS}$ profile reproduces the South China $\delta^{34}S_{CAS}$ trends for comparison. The South China profile is a composite of three sections: Dajiang (squares), Lower Guandao (circles), and Shitouzhai (inverted triangles; Section S3). CIEs are numbered per Song-HY et al. (2013), and the location of N3 was marked near the inflection point of the $\delta^{13}C_{carb}$ curve. Abbreviations: Sp. – Spathian; Dien. – Dienerian; PTB – Permian-Triassic Boundary.

6.3. Paleoenvironmental drivers

6.3.1. Global controls on $\delta^{34}S_{CAS}$ and $\delta^{18}O_{CAS}$

The positive correlation between $\delta^{34}S_{CAS}$ and $\delta^{18}O_{CAS}$ (r_s = +0.45; p-value < 0.001; Fig. 3F), reflected in strongly coupled fluctuations throughout the Early Triassic (Fig. 3), limits the range of viable mechanisms to explain secular variations in the marine sulfur cycle during this interval. Environmental scenarios that could have driven correlated changes in both $\delta^{34}S_{CAS}$ and

 $\delta^{18}O_{CAS}$ include variation in (1) sulfate inputs from continental weathering or volcanism, and (2) changes in net marine MSR.

Riverine sulfate fluxes would have had to have weakened in order to account for positive CAS-isotope excursions around the Griesbachian-Dienerian boundary, Dienerian-Smithian boundary, and Smithian-Spathian boundary. Both source fluxes, i.e., subaerial weathering and volcanic emissions, produce sulfate that is relatively ³⁴S- and ¹⁸O-depleted, so increasing (decreasing) fluxes from these sources would decrease (increase) the $\delta^{34}S_{CAS}$ and $\delta^{18}O_{CAS}$ values of seawater sulfate (Newton et al., 2004; Bottrell and Newton, 2006). Oxidation of pyrite during continental weathering produces sulfate that is ³⁴S-depleted owing to the light S-isotopic composition of pyrite and ¹⁸O-depleted owing to incorporation of oxygen from meteoric waters (Bottrell and Newton, 2006). Mercury concentration data suggest that there were increased volcanic inputs during the late Smithian (Grasby et al., 2013b, 2015), but otherwise there is little evidence for further major eruptive phases of the Siberian Traps after the Griesbachian (Burgess and Bowring, 2015). On the other hand, global changes in weathering intensity during the Early Triassic have been inferred based on carbonate 87Sr/86Sr isotopes that broadly correlate with fluctuations in sea-surface temperatures and marine redox conditions (Sedlacek et al., 2014; Zhang et al., 2018; note the conodont ⁸⁷Sr/⁸⁶Sr record of Song-HJ et al., 2015 is too lowresolution to capture short-term events in the Griesbachian to Smithian). Both $\delta^{34}S_{CAS}$ and $\delta^{18}O_{CAS}$ tended to decrease during episodes of Early Triassic warming (Fig. 3), consistent with the hypothesis that changes in weathering intensity controlled secular $\delta^{34}S_{CAS}$ and $\delta^{18}O_{CAS}$ variation. However, Early Triassic weathering rates appear to vary at a global scale (e.g., Lehrmann et al., 2015; Wei et al., 2015b), complicating interpretation of their significance as a control on $\delta^{34}S_{CAS}$ and $\delta^{18}O_{CAS}$ covariation.

The scenario that we suggest as the main control on covariation between $\delta^{34}S_{CAS}$ and $\delta^{18}O_{CAS}$ was changes in net marine MSR, i.e., the difference between the forward MSR process and the reverse sulfide oxidation process. Under this scenario, increased net MSR led to increased $\delta^{34}S_{CAS}$ and $\delta^{18}O_{CAS}$ values, and vice versa. A net MSR increase could have been due either to increased MSR rates or to decreased sulfide oxidation rates. Differentiating between these two possibilities is difficult, but data concerning Early Triassic marine productivity is relevant because the MSR process is organic matter-limited (Bottrell and Newton, 2006). In the Early Triassic, sediment $\delta^{13}C_{carb}$ and TOC values likely reflect burial fluxes of organic carbon linked to primary productivity (Algeo et al., 2011, 2013; Song-HY et al., 2013, 2014). During three intervals of increased $\delta^{13}C_{carb}$, higher productivity, and organic carbon burial around the Griesbachian-Dienerian boundary, Dienerian-Smithian boundary, and Smithian-Spathian boundary, values of $\delta^{34}S_{CAS}$ and $\delta^{18}O_{CAS}$ also increased. Close coupling between carbonate $\delta^{13}C$ and sulfate δ^{34} S- δ^{18} O was possible during the Early Triassic due to drawdown in seawater sulfate concentrations producing similar residence times, ~200 kyr, for seawater sulfate and dissolved inorganic carbon (Song-HY et al., 2014). This link suggests that covariation between $\delta^{34}S_{CAS}$ and $\delta^{18}O_{CAS}$ in the Early Triassic was controlled by net global MSR changes linked to organic matter availability, in agreement with the scenario initially proposed by Song-HY et al. (2014) based on $\delta^{34}S_{CAS}$ data from the eastern Paleo-Tethys.

6.3.2. Local controls on $\delta^{34}S_{pyr}$ and $\Delta^{34}S_{CAS-pyr}$

Potential environmental changes and drivers of the Early Triassic marine sulfur cycle within the southern Neo-Tethys can be inferred on the basis of $\delta^{34}S_{pyr}$ data in combination with $\delta^{34}S_{CAS}$ and $\delta^{13}C_{carb}$. $\Delta^{34}S_{CAS-pyr}$ (i.e., the difference between $\delta^{34}S_{CAS}$ and $\delta^{34}S_{pyr}$) is influenced by

multiple factors related to MSR and the formation and burial of pyrite. These factors include the MSR rate (Leavitt et al., 2013), the location of the MSR zone relative to the supply of sulfate (open- or closed-system systems; e.g., Gomes and Hurtgen, 2015), and seawater sulfate concentrations (Algeo et al., 2015). Maxima in $\Delta^{34}S_{CAS-pvr}$ are observed close to the Dienerian-Smithian boundary and the Smithian-Spathian boundary, coincident with positive CIEs (Fig. 3). A discrepancy currently occurs near the Griesbachian-Dienerian boundary where the $\Delta^{34}S_{CAS-pvr}$ maximum occurs within the positive CIE but below the maximum $\delta^{13}C_{carb}$ value (Fig. 3). This difference could be due to many factors including the condensed nature of this part of the Spiti Valley sections (Fig. S4), errors in correlating the sections for the composite curve (Section 3), or sample-to-sample variability and the lower-resolution data of the Griesbachian and Dienerian substages (Section 6.1). Further work around the Griesbachian-Dienerian boundary with a less condensed section and higher-resolution data is needed to elucidate the exact timing of the $\Delta^{34}S_{CAS-pvr}$ maximum within the positive CIE. Furthermore, like $\delta^{13}C_{carb}$, $\Delta^{34}S_{CAS-pvr}$ decreased from the mid-Dienerian to earliest Smithian and, with greater variability, from the early to latest Smithian.

The likely paleoenvironmental driver controlling Spiti Valley $\Delta^{34}S_{CAS-pyr}$ values was the location of the MSR zone and resulting changes in open- or closed-system conditions (Fig. 8; see Section S5 for further discussion on ruling out the rate of MSR and sulfate concentrations). When MSR occurs under open-system conditions, typically in the water column or within the sediments near the sediment-water interface, it is not limited by aqueous sulfate availability, and $\Delta^{34}S_{CAS-pyr}$ will be larger owing to little or no Rayleigh distillation (e.g., Gomes and Hurtgen, 2015). On the other hand, when MSR occurs under closed-system conditions, porewater sulfate is not replenished, and continued MSR results in increasingly higher $\delta^{34}S_{pyr}$ values relative to

open-system conditions. Based on the results at Spiti Valley, MSR occurred under more open-system conditions during the positive CIEs than during intervals of low δ^{13} C (Fig. 8).

Several lines of evidence favor open- versus closed-system conditions as the main control on Lower Triassic $\delta^{34}S_{pyr}$ values in the southern Neo-Tethys. First, pyrite morphology changes as a function of the location of the MSR zone. When MSR occurs within the water column (syngenetic) or close to the sediment-water interface (early diagenetic), pyrite crystallizes primarily in a framboidal form (Wilkin et al., 1996; Bond and Wignall, 2010). In contrast, euhedral pyrite forms during later diagenesis and dominates when the location of the MSR zone is deeper below the sediment-water interface. Therefore, the dominance of framboidal pyrite in the present study units suggests that MSR occurred in the water column or within the sediments near the sediment-water interface and, thus, under relatively open-system conditions. At Spiti Valley, framboidal pyrite is most abundant within the Griesbachian to lower Dienerian and uppermost Smithian, with a slight increase also in the lower Smithian (Fig. 4B). All three intervals are characterized by lower $\delta^{34}S_{pyr}$ values and relative increases in $\Delta^{34}S_{CAS-pyr}$, consistent with more open-system conditions.

A second line of evidence is the relationship between S_{pyr} and $\delta^{34}S_{pyr}$, which can provide an estimate of the relative amounts of S-isotopic compositions of the syngenetic and diagenetic fractions of whole-rock pyrite (Algeo et al., 2007, 2008). For example, data from the Nhi Tao, Vietnam and Xiaojiaba, South China P-Tr boundary sections document two-component mixing trends between a syngenetic pyrite endmember with low $\delta^{34}S$ and a diagenetic pyrite endmember with high $\delta^{34}S$ (Algeo et al., 2008; Wei et al., 2015a; but note that some P-Tr boundary sections contain more than two pyrite fractions, e.g., Shen et al., 2016). The Spiti Valley section exhibits a pattern of negative S_{pyr} - $\delta^{34}S_{pyr}$ covariation ($r_s = -0.57$, p-value < 0.001) that is consistent with

two-component mixing (Fig. 4C), yielding estimates of ca. -20 % and +20 to +25 % for the syngenetic and diagenetic pyrite fractions, respectively. This suggests that bulk-sample $\delta^{34}S_{pyr}$ reflects local changes in the proportions of syngenetic and diagenetic pyrite and, therefore, in the location of the MSR zone.

Although the primary control on $\Delta^{34}S_{CAS-pvr}$ trends at Spiti Valley was the location of the MSR zone, a secondary factor that affected absolute $\Delta^{34}S_{CAS-pvr}$ values was seawater sulfate concentrations. Paleo-seawater sulfate concentrations can be estimated using the "MSR-trend" method, which relies on the relation between MSR fractionation, proxied by $\Delta^{34}S_{CAS,pyr}$, and seawater sulfate concentrations (Algeo et al., 2015). Estimates of Early Triassic seawater sulfate concentrations using the "MSR-trend" method suggest there was a broad increase from the P-Tr boundary (<3 mM; Schobben et al., 2017) to the Smithian-Spathian boundary (<9 mM; Stebbins et al., in press). Furthermore, using the rate method of Algeo et al. (2015), a similar range of sulfate concentrations (2-6 mM) was estimated for the Griesbachian and Dienerian, followed by a rise to 10-15 mM in the Middle Triassic, based on the evaporite compilation of Bernasconi et al. (2017). For the Spiti Valley, substage-level median $\Delta^{34}S_{CAS-pyr}$ values imply an increase in seawater sulfate concentrations during the Early Triassic: Griesbachian (5.0 mM), Dienerian (5.4 mM), Smithian (7.8 mM), and early Spathian (9.9 mM; Fig. 9). The gradual increase in Δ^{34} S_{CAS}. pyr is consistent with a slow rise in seawater sulfate concentrations from one substage to the next. Moreover, the convergence in the $\delta^{34}S_{CAS}$ profiles of the Spiti Valley and South China sections by the Smithian argues for growth of the seawater sulfate pool to a level that homogenized sulfate $\delta^{34}S$ globally (Section 6.2). This provides confidence in the inferred trend of slowly rising seawater sulfate concentrations even though the number of samples for each substage is relatively low and the $\Delta^{34}S_{CAS-pvr}$ variance large, which was likely due to variations in open-

versus closed-system conditions. However, further studies of Early Triassic seawater sulfate concentrations will be needed to confirm these inferences.

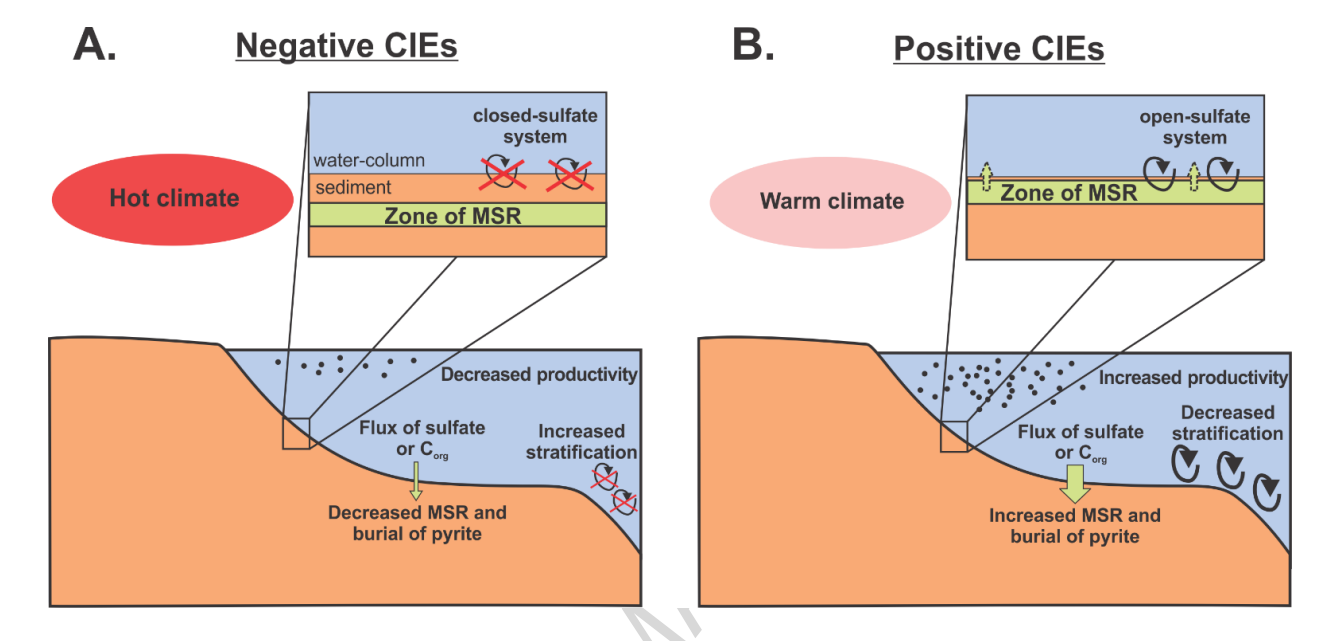


Figure 8. Generalized representation of environmental changes at Spiti Valley during (A) negative CIEs and (B) positive CIEs (described in Section 6.4). During the positive CIEs, decreased temperatures led to decreased stratification, and increased productivity and organic matter availability. With increased organic matter availability and microbial respiration, the zone of MSR shallowed toward the sediment-water interface, increasing sulfate availability and leading to increased MSR and pyrite burial. The opposite occurred during the negative CIEs.

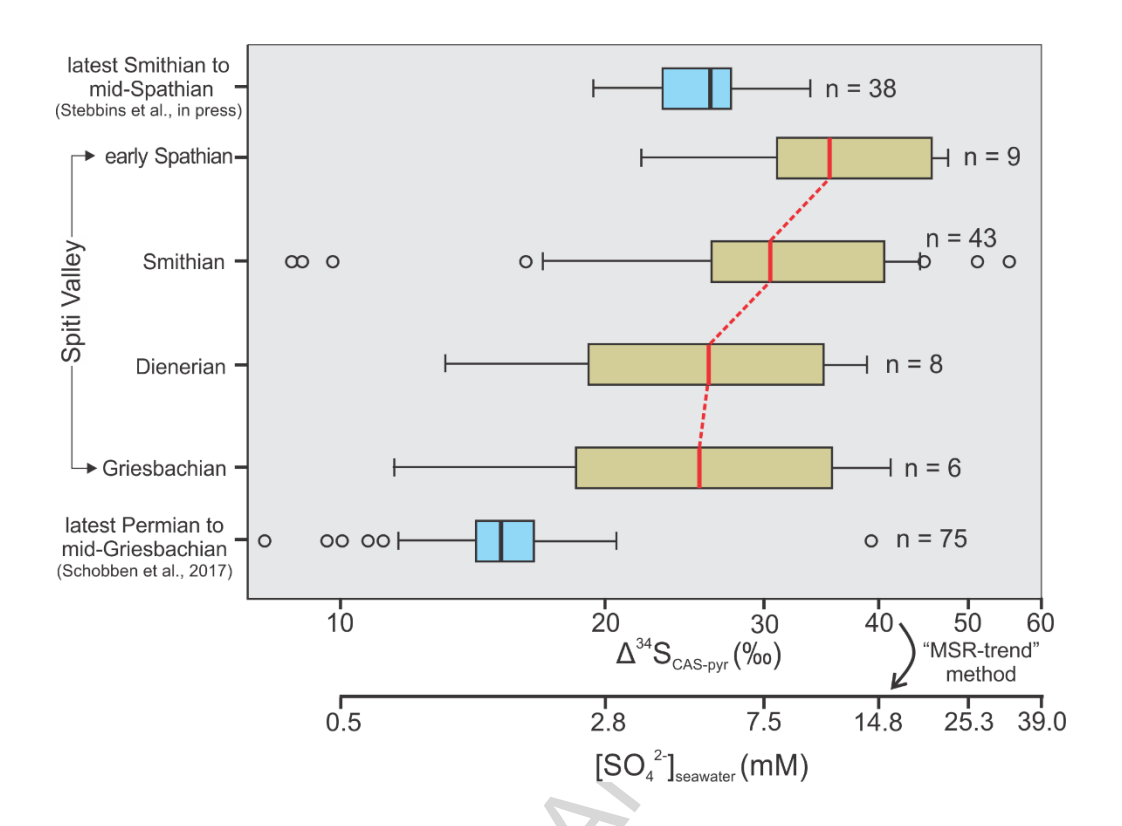


Figure 9. Spiti Valley $\Delta^{34}S_{CAS-pyr}$ compiled at the substage level. We estimated Early Triassic seawater sulfate concentrations using each substage's median $\Delta^{34}S_{CAS-pyr}$ (solid red line) and the "MSR-trend" method (Algeo et al., 2015). There was an increase in median $\Delta^{34}S_{CAS-pyr}$ substage values, and therefore seawater sulfate concentrations, from the Griesbachian to early Spathian (Griesbachian: +26.1 ‰, 5.4 mM; Dienerian: +26.3 ‰, 5.4 mM; Smithian: +31.0 ‰, 8.1 mM; and early Spathian: +36.8 ‰, 12.2 mM). For comparison to Spiti Valley, we show the distribution of $\Delta^{34}S_{CAS-pyr}$ from Hungarian and Iranian sections for the latest Permian (conodont zone *Clarkina yini*) to mid-Griesbachian (conodont zone *Isarcicella isarcica*; Schobben et al., 2017) and the Jesmond, western Canadian section for the latest Smithian to mid-Spathian (Stebbins et al., in press). It is important to note that the Jesmond samples may represent conservative estimates of seawater sulfate concentrations due to possibly closed sulfate system dynamics (Stebbins et al., in press).

6.4. Environmental conditions during the Early Triassic recovery

Similar to the eastern Paleo-Tethys region (Song-HY et al., 2014), our results document strong links between the Early Triassic marine carbon and sulfur cycles in the southern Neo-

Tethys Ocean. We conclude, like Song-HY et al. (2014), that coupled burial rates of pyrite and organic carbon controlled isotope variation due to environmental factors such as temperature, productivity, and oceanic circulation (Fig. 8). Furthermore, our paired $\delta^{18}O_{CAS}$, $\delta^{34}S_{pyr}$, and $\Delta^{34}S_{CAS-pyr}$ records allow us to further characterize the environmental processes involved in this scenario. We suggest that the global pyrite burial flux was controlled by changes to net MSR which, in turn, was facilitated in the southern Neo-Tethys by changes in sulfate availability related to the location of the MSR zone (i.e., in the water column versus in the sediment; Fig. 8).

In detail, our CAS and pyrite-isotope data show that the highest burial rates of pyrite occurred when sulfate availability was unlimited owing to MSR in the water column or close to the sediment-water interface (Fig. 3). Sea-surface temperatures (Sun et al., 2012; Romano et al., 2013) appear to correlate strongly with this process, and the highest global burial rates of pyrite occurred during relatively cooler intervals (Song-HY et al., 2014). Mechanistically, climatic cooling steepens equator-to-pole temperature gradients, leading to invigorated thermohaline overturning circulation in the global ocean (Ganachaud and Wunsch, 2000; Clark et al., 2002; Stouffer et al., 2006; Sinninghe Damsté et al., 2010; Linnert et al., 2014). Enhanced circulation brings more nutrients from deep waters into the ocean-surface layer via upwelling, therefore, stimulating marine productivity (Sarmiento et al., 2003; Whitney et al., 2005). Enhanced productivity fueled and sustained microbial respiration, increased oxygen demand, and, within the southern Neo-Tethys, caused the zone of MSR to migrate upwards and become more connected to the water column. MSR, under these conditions, was no longer limited by organic matter or sulfate availability, leading to burial of more ³⁴S-depleted pyrite and ³⁴S- and ¹⁸Oenrichment of the oceanic sulfate pool. In contrast, during the warmer intervals of decreased organic matter flux to the sediments, our data show decreased microbial respiration that pushed

the zone of MSR into the sediments, limiting sulfate supply through diffusion from the water column. MSR under closed-system conditions limited pyrite formation while increasing $\delta^{34}S_{pyr}$ due to Rayleigh distillation.

Our data suggest the possible development of eutrophic conditions in the southern Neo-Tethys during the recurring positive CIEs. Eutrophication as an environmental stressor during the Early Triassic recovery was inferred for the western Paleo-Tethys region (i.e., Hungary) for the entire Griesbachian to Smithian interval based on benthic community structure (Foster et al., 2015). Although riverine nutrient fluxes can be locally important on modern continental shelves, the bulk of ocean-surface nutrients is supplied via upwelling from intermediate oceanic depths (Chen and Wang, 1999; Liu et al., 2010). Consistent with this relationship, our data suggest that Early Triassic marine eutrophication was driven largely by changes in ocean stratification and nutrient cycling during intervals of relative cooling. This contrasts with the shorter end-Permian mass extinction interval, when eutrophication was possibly driven by increased continental weathering during a hyperwarming event (Algeo and Twitchett, 2010; Joachimski et al., 2012; Schoepfer et al., 2013; Schobben et al., 2014; Schobben et al., 2015; Kaiho et al., 2016). However, the influence of ocean circulation and stratification on marine nutrient budgets likely outweighed the effects of continental weathering changes in terms of stimulating primary production, microbial respiration, and potential eutrophication for most of the Early Triassic. This inference is supported by data from the western margin of Pangea (i.e., the Opal Creek section), which recorded a transient eutrophic interval during the end-Permian extinction interval but a subsequent shutdown of upwelling and a major decline of productivity during the Early Triassic in response to hyperwarming (Schoepfer et al., 2013).

The overall low abundance of framboidal pyrite at Spiti Valley compared to other Lower Triassic sections (e.g., Wignall et al., 2015; Huang et al., 2017) suggests that sedimentation on the southern Neo-Tethys shelf was mostly under oxic conditions. However, reduced oxygen availability may have been associated with two of the three positive CIEs, i.e., around the Griesbachian-Dienerian and Smithian-Spathian boundaries, based on framboid size distributions (Fig. 4D). Other Neo-Tethyan sections, e.g., on the Northern Indian Margin (Galfetti et al., 2007a) and the Arabian Margin (Clarkson et al., 2016), show evidence of more severe oxygen depletion during the Dienerian-Smithian and Smithian-Spathian positive CIEs. However, the Griesbachian-Dienerian positive CIE was associated with relatively well-oxygenated conditions on the Arabian Margin (Clarkson et al., 2016). On a global scale, oceanic oxygen availability was spatially heterogeneous throughout the Early Triassic (Wignall et al., 2010; Song-HJ et al., 2012; Grasby et al., 2013a; Metcalfe et al., 2013; Feng and Algeo, 2014; Tian et al., 2014; Sun et al., 2015; Takahashi et al., 2015; Wei et al., 2015b; Wignall et al., 2015; Huang et al., 2017).

In view of pronounced local redox variability during the Early Triassic, carbonate uranium isotopes are proving to be a valuable proxy for assessing secular variations in global-average ocean redox conditions. A high-resolution U-isotope dataset from Zal, Iran provided evidence of globally more extensive oceanic anoxia during negative CIEs than during positive CIEs of the Early Triassic, reflecting severe stagnation of global-ocean circulation during the hyperwarming events linked to negative CIEs (Zhang et al., 2018). These relationships have counterparts in the Cretaceous OAE2, which shows major perturbations to global carbon and sulfur cycles (Gomes et al., 2016 and references therein). The environmental scenario proposed here (Fig. 8) does not necessarily require an anoxic water column during the positive CIEs. Pyrite burial during the positive CIEs increased owing to greater sulfate availability in an open system, associated with

MSR either close to the sediment-water interface of an oxic water column or within an anoxic water column.

The positive CIEs of the Early Triassic were the intervals associated with biotic recovery in both the terrestrial (Hochuli et al., 2016 and references therein) and marine realms (Brayard et al., 2006, 2017; Orchard, 2007; Stanley, 2009). This biodiversity pattern coupled to carbon cycle perturbations was confirmed locally in the southern Neo-Tethys from ammonoid diversity patterns in the Dienerian and Smithian substages (Brühwiler et al., 2010a; Ware et al., 2015). This pattern suggests that the increased temperatures during the negative CIEs were more harmful to biodiversity, but were also the intervals with globally reduced organic matter and pyrite burial. It should be noted that decreases in organic carbon and pyrite burial do not necessarily imply a reduction in the global extent of oceanic anoxia. Rather, it merely suggests a global decrease in MSR limited by the availability of reactants like organic matter. During Early Triassic hyperwarming intervals, the environmental mechanisms leading to oxygen limitation likely switched from increased productivity and organic matter respiration to stagnant water columns and decreased oxygen solubility (Song-HY et al., 2013; Wei et al., 2015b). In this context, the environmental processes and stresses related to temperature increases seemed to have exerted more control on marine biodiversity and recovery following the end-Permian mass extinction than any potential stresses due to eutrophication (Stanley et al., 2009; Sun et al., 2012). Hyperwarming would have led to decreased marine habitat variability (Galfetti et al., 2007b) and shrunk the marine habitable zone (Beatty et al., 2008; Song-HJ et al., 2014). The harshness of marine environmental would have peaked when both factors, eutrophication and temperature increases, worked in tandem (e.g., Schobben et al., 2015).

7. Conclusions

The $\delta^{34}S_{CAS}$ trends from the southern Neo-Tethys (Spiti Valley) record global changes to the Early Triassic marine sulfur cycle during the Griesbachian to early Spathian. Linked changes between $\delta^{34}S_{CAS}$ and $\delta^{13}C_{carb}$ confirm the hypothesis that global fluctuations in organic matter and pyrite burial occurred throughout the Early Triassic. Further constraints on pyrite burial rates were provided by $\delta^{18}O_{CAS}$, $\delta^{34}S_{pyr}$, and $\Delta^{34}S_{CAS-pyr}$. These data imply increased MSR on a global scale combined with a shallowing of the local zone of MSR in the southern Neo-Tethys during intervals characterized by positive CIEs (i.e., around the Griesbachian-Dienerian, Dienerian-Smithian, and Smithian-Spathian boundaries). Additionally, median $\Delta^{34}S_{CAS-pyr}$ values gradually increased from the Griesbachian to early Spathian suggesting a slow rise in seawater sulfate concentrations during the Early Triassic.

We conclude that the most likely mechanism contributing to increased pyrite burial during positive CIEs involved climatic cooling, invigorated oceanic overturning circulation, increased nutrient cycling to the surface ocean, and enhanced primary productivity and organic matter fluxes to the sediment. The latter stimulated and maintained microbial respiration. Thus, our data are consistent with the development of eutrophic conditions in the southern Neo-Tethys during positive CIEs of the Early Triassic. The environmental scenario presented here suggests that CAS and pyrite isotopes reflected organic matter availability that did not explicitly require a change in water-column oxygen availability but a change in how the zone of MSR interacted with the water-column sulfate supply.

Acknowledgments

The authors thank Dr. Ron Blakey for developing and allowing use of the Early Triassic paleogeographic map. AS thanks the School for the Environment's Environmental Analytical Facility at UMass Boston (NSF Award # 09-42371; DBI:MRI-RI2; PIs: RH and Dr. Alan Christian) for access to analytical instrumentation. AS gratefully acknowledges support by the National Science Foundation Graduate Research Fellowship (DGE-1356104), UMass Boston Chancellor's Distinguished Doctoral Fellowship, and UMass Boston's School for the Environment. TJA thanks the Sedimentary Geology and Paleobiology program of the U.S. National Science Foundation, the NASA Exobiology program, and the China University of Geosciences-Wuhan (SKL-GPMR program GPMR201301, and SKL-BGEG program BGL21407) for research support. Thanks to Sylvain Richoz for editorial handling and to Ulrich Wortmann and Pedro Marenco for constructive reviews of the original manuscript.

References

- Algeo, T. J., and Twitchett, R. J., 2010, Anomalous Early Triassic sediment fluxes due to elevated weathering rates and their biological consequences: Geology, v. 38, no. 11, p. 1023-1026.
- Algeo, T. J., Ellwood, B., Nguyen, T. K. T., Rowe, H., and Maynard, J. B., 2007, The Permian—Triassic boundary at Nhi Tao, Vietnam: evidence for recurrent influx of sulfidic watermasses to a shallow-marine carbonate platform: Palaeogeography, Palaeocclimatology, Palaeoecology, v. 252, no. 1, p. 304-327.
- Algeo, T. J., Shen, Y., Zhang, T., Lyons, T., Bates, S., Rowe, H., and Nguyen, T. K. T., 2008, Association of 34 S-depleted pyrite layers with negative carbonate δ^{13} C excursions at the Permian-Triassic boundary: Evidence for upwelling of sulfidic deep-ocean water masses: Geochemistry, Geophysics, Geosystems, v. 9, no. 4, p. 1-10.
- Algeo, T. J., Chen, Z. Q., Fraiser, M. L., and Twitchett, R. J., 2011, Terrestrial-marine teleconnections in the collapse and rebuilding of Early Triassic marine ecosystems: Palaeogeography, Palaeoclimatology, Palaeoecology, v. 308, no. 1–2, p. 1-11.
- Algeo, T. J., Henderson, C. M., Tong, J., Feng, Q., Yin, H., and Tyson, R. V., 2013, Plankton and productivity during the Permian–Triassic boundary crisis: an analysis of organic carbon fluxes: Global and Planetary Change, v. 105, p. 52-67.
- Algeo, T. J., Luo, G. M., Song, H. Y., Lyons, T. W., and Canfield, D. E., 2015, Reconstruction of secular variation in seawater sulfate concentrations: Biogeosciences, v. 12, no. 7, p. 2131-2151.

- Balci, N., Shanks, W. C., III, Mayer, B., and Mandernack, K. W., 2007, Oxygen and sulfur isotope systematics of sulfate produced by bacterial and abiotic oxidation of pyrite: Geochimica et Cosmochimica Acta, v. 71, no. 15, p. 3796-3811.
- Balci, N., Mayer, B., Shanks, W. C., III, and Mandernack, K. W., 2012, Oxygen and sulfur isotope systematics of sulfate produced during abiotic and bacterial oxidation of sphalerite and elemental sulfur: Geochimica et Cosmochimica Acta, v. 77, p. 335-351.
- Beatty, T. W., Zonneveld, J.-P., and Henderson, C. M., 2008, Anomalously diverse Early Triassic ichnofossil assemblages in northwest Pangea: A case for a shallow-marine habitable zone: Geology, v. 36, no. 10, p. 771-774.
- Bernasconi, S. M., Meier, I., Wohlwend, S., Brack, P., Hochuli, P. A., Bläsi, H., Wortmann, U. G., and Ramseyer, K., 2017, An evaporite-based high-resolution sulfur isotope record of Late Permian and Triassic seawater sulfate: Geochimica et Cosmochimica Acta, v. 204, p. 331-349.
- Bhargava, O. N., 2008, An updated introduction to the Spiti Geology: Journal of the Palaeontological Society of India, v. 53, no. 2, p. 113-128.
- Bhargava, O. N., Krystyn, L., Balini, M., Lein, R., and Nicora, A., 2004, Revised litho- and sequence stratigraphy of the Spiti Triassic: Albertiana, v. 30, p. 21-39.
- Bond, D. P. G., and Wignall, P. B., 2010, Pyrite framboid study of marine Permian—Triassic boundary sections: A complex anoxic event and its relationship to contemporaneous mass extinction: Geological Society of America Bulletin, v. 122, no. 7-8, p. 1265-1279.
- Böttcher, M. E., and Thamdrup, B., 2001, Anaerobic sulfide oxidation and stable isotope fractionation associated with bacterial sulfur disproportionation in the presence of MnO₂: Geochimica et Cosmochimica Acta, v. 65, no. 10, p. 1573-1581.
- Böttcher, M. E., Thamdrup, B., Gehre, M., and Theune, A., 2005, ³⁴S/³²S and ¹⁸O/¹⁶O Fractionation during sulfur disproportionation by *Desulfobulbus propionicus*: Geomicrobiology Journal, v. 22, no. 5, p. 219-226.
- Bottrell, S. H., and Newton, R. J., 2006, Reconstruction of changes in global sulfur cycling from marine sulfate isotopes: Earth-Science Reviews, v. 75, no. 1–4, p. 59-83.
- Bowles, M. W., Mogollón, J. M., Kasten, S., Zabel, M., and Hinrichs, K.-U., 2014, Global rates of marine sulfate reduction and implications for sub-sea-floor metabolic activities: Science, v. 344, no. 6186, p. 889-891.
- Brayard, A., Bucher, H., Escarguel, G., Fluteau, F., Bourquin, S., and Galfetti, T., 2006, The Early Triassic ammonoid recovery: Paleoclimatic significance of diversity gradients: Palaeogeography, Palaeoclimatology, Palaeoecology, v. 239, no. 3–4, p. 374-395.
- Brayard, A., Krumenacker, L. J., Botting, J. P., Jenks, J. F., Bylund, K. G., Fara, E., Vennin, E., Olivier, N., Goudemand, N., Saucede, T., Charbonnier, S., Romano, C., Doguzhaeva, L., Thuy, B., Hautmann, M., Stephen, D. A., Thomazo, C., and Escarguel, G., 2017, Unexpected Early Triassic marine ecosystem and the rise of the Modern evolutionary fauna: Science Advances, v. 3, no. 2, e1602159.
- Brühwiler, T., Bucher, H., Brayard, A., and Goudemand, N., 2010a, High-resolution biochronology and diversity dynamics of the Early Triassic ammonoid recovery: The Smithian faunas of the Northern Indian Margin: Palaeogeography, Palaeoclimatology, Palaeoecology, v. 297, no. 2, p. 491-501.
- Brühwiler, T., Ware, D., Bucher, H., Krystyn, L., and Goudemand, N., 2010b, New Early Triassic ammonoid faunas from the Dienerian/Smithian boundary beds at the

- Induan/Olenekian GSSP candidate at Mud (Spiti, Northern India): Journal of Asian Earth Sciences, v. 39, no. 6, p. 724-739.
- Brühwiler, T., Bucher, H., and Krystyn, L., 2012, Middle and late Smithian (Early Triassic) ammonoids from Spiti, India. In: Brühwiler, T., and Bucher, H. (eds.), Smithian (Early Triassic) Ammonoids from the Salt Range (Pakistan) and Spiti (India), Special Papers in Palaeontology no. 88, p. 119-174.
- Brunner, B., Bernasconi, S. M., Kleikemper, J., and Schroth, M. H., 2005, A model for oxygen and sulfur isotope fractionation in sulfate during bacterial sulfate reduction processes: Geochimica et Cosmochimica Acta, v. 69, no. 20, p. 4773-4785.
- Burdett, J., Arthur, A., and Richardson, M., 1989, A Neogene seawater sulfur isotope age curve from calcareous pelagic microfossils: Earth and Planetary Science Letters, v. 94, no. 3, p. 189-198.
- Burgess, S. D., and Bowring, S. A., 2015, High-precision geochronology confirms voluminous magmatism before, during, and after Earth's most severe extinction: Science Advances, v. 1, no. 7, e1500470.
- Burgess, S. D., Bowring, S., and Shen, S. Z., 2014, High-precision timeline for Earth's most severe extinction: Proceedings of the National Academy of Sciences (U.S.A.), v. 111, no. 9, p. 3316-3321.
- Burgess, S. D., Muirhead, J. D., and Bowring, S. A., 2017, Initial pulse of Siberian Traps sills as the trigger of the end-Permian mass extinction: Nature Communications, v. 8, no. 164, p. 1-6
- Butler, I. B., Böttcher, M. E., Rickard, D., and Oldroyd, A., 2004, Sulfur isotope partitioning during experimental formation of pyrite via the polysulfide and hydrogen sulfide pathways: implications for the interpretation of sedimentary and hydrothermal pyrite isotope records: Earth and Planetary Science Letters, v. 228, no. 3–4, p. 495-509.
- Canfield, D. E., 1991, Sulfate reduction in deep-sea sediments: American Journal of Science, v. 291, no. 2, p. 177-188.
- Canfield, D. E., 2001, Isotope fractionation by natural populations of sulfate-reducing bacteria: Geochimica et Cosmochimica Acta, v. 65, no. 7, p. 1117-1124.
- Canfield, D. E., Raiswell, R., Westrich, J. T., Reaves, C. M., and Berner, R. A., 1986, The use of chromium reduction in the analysis of reduced inorganic sulfur in sediments and shales: Chemical Geology, v. 54, no. 1-2, p. 149-155.
- Canfield, D. E., Olesen, C. A., and Cox, R. P., 2006, Temperature and its control of isotope fractionation by a sulfate-reducing bacterium: Geochimica et Cosmochimica Acta, v. 70, no. 3, p. 548-561.
- Chen, C.-T. A., and Wang, S.-L., 1999, Carbon, alkalinity and nutrient budgets on the East China Sea continental shelf: Journal of Geophysical Research: Oceans, v. 104, no. C9, p. 20675-20686.
- Chen, Z.-Q., and Benton, M. J., 2012, The timing and pattern of biotic recovery following the end-Permian mass extinction: Nature Geoscience, v. 5, no. 6, p. 375-383.
- Clark, P.U., Pisias, N.G., Stocker, T.F., and Weaver, A.J., 2002. The role of the thermohaline circulation in abrupt climate change. Nature 415, 863-869.
- Clarkson, M. O., Wood, R. A., Poulton, S. W., Richoz, S., Newton, R. J., Kasemann, S. A., Bowyer, F., and Krystyn, L., 2016, Dynamic anoxic ferruginous conditions during the end-Permian mass extinction and recovery: Nature Communications, v. 7, no. 12236, p. 1-9.

- Claypool, G. E., Holser, W. T., Kaplan, I. R., Sakai, H., and Zak, I., 1980, The age curves of sulfur and oxygen isotopes in marine sulfate and their mutual interpretation: Chemical Geology, v. 28, p. 199-260.
- Cortecci, G., and Longinelli, A., 1971, ¹⁸O/¹⁶O ratios in sulfate from living marine organisms: Earth and Planetary Science Letters, v. 11, no. 1–5, p. 273-276.
- Cortecci, G., Reyes, E., Berti, G., and Casati, P., 1981, Sulfur and oxygen isotopes in Italian marine sulfates of Permian and Triassic ages: Chemical Geology, v. 34, no. 1–2, p. 65-79.
- Derry, L. A., Kaufman, A. J., and Jacobsen, S. B., 1992, Sedimentary cycling and environmental change in the Late Proterozoic: Evidence from stable and radiogenic isotopes: Geochimica et Cosmochimica Acta, v. 56, no. 3, p. 1317-1329.
- Erwin, D., 1994, The Permo-Triassic Extinction: Nature, v. 367, no. 6460, p. 231-236.
- Feng, Q. L., and Algeo, T. J., 2014, Evolution of oceanic redox conditions during the Permo-Triassic transition: Evidence from deepwater radiolarian facies: Earth-Science Reviews, v. 137, p. 34-51.
- Foster, W. J., Danise, S., Sedlacek, A., Price, G. D., Hips, K., and Twitchett, R. J., 2015, Environmental controls on the post-Permian recovery of benthic, tropical marine ecosystems in western Palaeotethys (Aggtelek Karst, Hungary): Palaeogeography, Palaeoclimatology, Palaeoecology, v. 440, p. 374-394.
- Fritz, P., Basharmal, G. M., Drimmie, R. J., Ibsen, J., and Qureshi, R. M., 1989, Oxygen isotope exchange between sulphate and water during bacterial reduction of sulphate: Chemical Geology, v. 79, no. 2, p. 99-105.
- Galfetti, T., Bucher, H., Brayard, A., Hochuli, P. A., Weissert, H., Guodun, K., Atudorei, V., and Guex, J., 2007a, Late Early Triassic climate change: Insights from carbonate carbon isotopes, sedimentary evolution and ammonoid paleobiogeography: Palaeogeography, Palaeoclimatology, Palaeoecology, v. 243, no. 3–4, p. 394-411.
- Galfetti, T., Hochuli, P. A., Brayard, A., Bucher, H., Weissert, H., and Vigran, J. O., 2007b, Smithian-Spathian boundary event: Evidence for global climatic change in the wake of the end-Permian biotic crisis: Geology, v. 35, no. 4, p. 291-294.
- Ganachaud, A., and Wunsch, C., 2000. Improved estimates of global ocean circulation, heat transport and mixing from hydrographic data. Nature 408, 453-457.
- Gill, B. C., Lyons, T. W., and Frank, T. D., 2008, Behavior of carbonate-associated sulfate during meteoric diagenesis and implications for the sulfur isotope paleoproxy: Geochimica et Cosmochimica Acta, v. 72, no. 19, p. 4699-4711.
- Gomes, M. L., and Hurtgen, M. T., 2015, Sulfur isotope fractionation in modern euxinic systems: Implications for paleoenvironmental reconstructions of paired sulfate-sulfide isotope records: Geochimica et Cosmochimica Acta, v. 157, p. 39-55.
- Gomes, M. L., Hurtgen, M. T., and Sageman, B. B., 2016, Biogeochemical sulfur cycling during Cretaceous oceanic anoxic events: A comparison of OAE1a and OAE2: Paleoceanography, v. 31, no. 2, p. 233-251.
- Gorjan, P., Kaiho, K., Kakegawa, T., Niitsuma, S., Chen, Z. Q., Kajiwara, Y., and Nicora, A., 2007, Paleoredox, biotic and sulfur-isotopic changes associated with the end-Permian mass extinction in the western Tethys: Chemical Geology, v. 244, no. 3–4, p. 483-492.
- Goudemand, N., 2014, Note on the conodonts from the Induan-Olenekian boundary: Albertiana, v. 42, p. 49-51.

- Grasby, S. E., Beauchamp, B., Embry, A., and Sanei, H., 2013a, Recurrent Early Triassic ocean anoxia: Geology, v. 41, no. 2, p. 175-178.
- Grasby, S. E., Sanei, H., Beauchamp, B., and Chen, Z., 2013b, Mercury deposition through the Permo-Triassic Biotic Crisis: Chemical Geology, v. 351, p. 209-216.
- Grasby, S. E., Beauchamp, B., Bond, D. P. G., Wignall, P. B., and Sanei, H., 2015, Mercury anomalies associated with three extinction events (Capitanian Crisis, Latest Permian Extinction and the Smithian/Spathian Extinction) in NW Pangea: Geological Magazine, v. 153, no. 2, p. 285-297.
- Hermann, E., Hochuli, P. A., Bucher, H., Brühwiler, T., Hautmann, M., Ware, D., Weissert, H., Roohi, G., and Yaseen, A., 2012, Climatic oscillations at the onset of the Mesozoic inferred from palynological records from the North Indian Margin: Journal of the Geological Society of London, v. 169, no. 2, p. 227-237.
- Hochuli, P. A., Sanson-Barrera, A., Schneebeli-Hermann, E., and Bucher, H., 2016, Severest crisis overlooked—Worst disruption of terrestrial environments postdates the Permian—Triassic mass extinction: Scientific Reports, v. 6, 28372.
- Holser, W. T., 1977, Catastrophic chemical events in the history of the ocean: Nature, v. 267, no. 5610, p. 403-408.
- Horacek, M., Brandner, R., and Abart, R., 2007a, Carbon isotope record of the P/T boundary and the Lower Triassic in the Southern Alps: Evidence for rapid changes in storage of organic carbon: Palaeogeography, Palaeoclimatology, Palaeoecology, v. 252, no. 1–2, p. 347-354.
- Horacek, M., Richoz, S., Brandner, R., Krystyn, L., and Spötl, C., 2007b, Evidence for recurrent changes in Lower Triassic oceanic circulation of the Tethys: The δ^{13} C record from marine sections in Iran: Palaeogeography, Palaeoclimatology, Palaeoecology, v. 252, no. 1–2, p. 355-369.
- Horacek, M., Koike, T., and Richoz, S., 2009, Lower Triassic δ^{13} C isotope curve from shallow-marine carbonates in Japan, Panthalassa realm: Confirmation of the Tethys δ^{13} C curve: Journal of Asian Earth Sciences, v. 36, no. 6, p. 481-490.
- Horacek, M., Brandner, R., Richoz, S., and Povoden-Karadeniz, E., 2010, Lower Triassic sulphur isotope curve of marine sulphates from the Dolomites, N-Italy: Palaeogeography, Palaeoclimatology, Palaeoecology, v. 290, no. 1–4, p. 65-70.
- Huang, Y. G., Chen, Z. Q., Wignall, P. B., and Zhao, L. S., 2017, Latest Permian to Middle Triassic redox condition variations in ramp settings, South China: Pyrite framboid evidence: Geological Society of America Bulletin, v. 129, no. 1-2, p. 229-243.
- Insalaco, E., Virgone, A., Courme, B., Gaillot, J., Kamali, M., Moallemi, A., Lotfpour, M., and Monibi, S., 2006, Upper Dalan Member and Kangan Formation between the Zagros Mountains and offshore Fars, Iran: depositional system, biostratigraphy and stratigraphic architecture: GeoArabia, v. 11, p. 74-176.
- Joachimski, M. M., Lai, X., Shen, S., Jiang, H., Luo, G., Chen, B., Chen, J., and Sun, Y., 2012, Climate warming in the latest Permian and the Permian-Triassic mass extinction: Geology, v. 40, no. 3, p. 195-198.
- Jorgensen, B. B., 1982, Mineralization of organic matter in the sea bed the role of sulphate reduction: Nature, v. 296, no. 5858, p. 643-645.
- Kaiho, K., Saito, R., Ito, K., Miyaji, T., Biswas, R., Tian, L., Sano, H., Shi, Z., Takahashi, S., Tong, J., Liang, L., Oba, M., Nara, F. W., Tsuchiya, N., and Chen, Z. Q., 2016, Effects of soil erosion and anoxic-euxinic ocean in the Permian-Triassic marine crisis: Heliyon, v. 2, no. 8, e00137.

- Kampschulte, A., and Strauss, H., 1998, The isotopic composition of trace sulphates in Paleozoic biogenic carbonates: implications for coeval seawater and geochemical cycles: Mineralogical Magazine, v. 62, p. 744-745.
- Kampschulte, A., and Strauss, H., 2004, The sulfur isotopic evolution of Phanerozoic seawater based on the analysis of structurally substituted sulfate in carbonates: Chemical Geology, v. 204, no. 3–4, p. 255-286.
- Kampschulte, A., Bruckschen, P., and Strauss, H., 2001, The sulphur isotopic composition of trace sulphates in Carboniferous brachiopods: implications for coeval seawater, correlation with other geochemical cycles and isotope stratigraphy: Chemical Geology, v. 175, no. 1, p. 149-173.
- Kaufman, A. J., and Knoll, A. H., 1995, Neoproterozoic variations in the C-isotopic composition of seawater: stratigraphic and biogeochemical implications: Precambrian Research, v. 73, no. 1–4, p. 27-49.
- Kaufman, A. J., Jacobsen, S. B., and Knoll, A. H., 1993, The Vendian record of Sr and C isotopic variations in seawater: Implications for tectonics and paleoclimate: Earth and Planetary Science Letters, v. 120, no. 3–4, p. 409-430.
- Krystyn, L., Balini, M., and Nicora, A., 2004, Lower and Middle Triassic stage and substage boundaries in Spiti: Albertiana, v. 30, p. 40-53.
- Krystyn, L., Bhargava, O., and Richoz, S., 2007a, A candidate GSSP for the base of the Olenekian Stage: Mud at Pin Valley; Himachal Pradesh (W. Himalaya), India: Albertiana, v. 35, p. 5-29.
- Krystyn, L., Richoz, S., and Bhargava, O., 2007b, The Induan-Olenekian Boundary (IOB) in Mud-an update of the candidate GSSP section M04: Albertiana, v. 36, p. 33-45.
- Leavitt, W. D., Halevy, I., Bradley, A. S., and Johnston, D. T., 2013, Influence of sulfate reduction rates on the Phanerozoic sulfur isotope record: Proceedings of the National Academy of Sciences (U.S.A.), v. 110, no. 28, p. 11244-11249.
- Lehrmann, D. J., Stepchinski, L., Altiner, D., Orchard, M. J., Montgomery, P., Enos, P., Ellwood, B. B., Bowring, S. A., Ramezani, J., Wang, H., Wei, J., Yu, M., Griffiths, J. D., Minzoni, M., Schaal, E. K., Li, X., Meyer, K. M., and Payne, J. L., 2015, An integrated biostratigraphy (conodonts and foraminifers) and chronostratigraphy (paleomagnetic reversals, magnetic susceptibility, elemental chemistry, carbon isotopes and geochronology) for the Permian–Upper Triassic strata of Guandao section, Nanpanjiang Basin, south China: Journal of Asian Earth Sciences, v. 108, p. 117-135.
- Linnert, C., Robinson, S. A., Lees, J. A., Bown, P. R., Pérez-Rodríguez, I., Petrizzo, M. R., Falzoni, F., Littler, K., Arz, J. A., and Russell, E. E., 2014. Evidence for global cooling in the Late Cretaceous. Nature Communications 5(4194), 1-7.
- Liu, K.-K., Atkinson, L., Quiñones, R. A., and Talaue-McManus, L., 2010, Biogeochemistry of continental margins in a global context. In: Liu, K.-K., Atkinson, L., Quiñones, R. A., Talaue-McManus, L. (eds) Carbon and Nutrient Fluxes in Continental Margins The IGBP Series, Springer, p. 3-24.
- Luo, G., Kump, L. R., Wang, Y., Tong, J., Arthur, M. A., Yang, H., Huang, J., Yin, H., and Xie, S., 2010, Isotopic evidence for an anomalously low oceanic sulfate concentration following end-Permian mass extinction: Earth and Planetary Science Letters, v. 300, no. 1–2, p. 101-111.
- Lyons, T. W., Walter, L. M., Gellatly, A. M., Martini, A. M., and Blake, R. E., 2004, Sites of anomalous organic remineralization in the carbonate sediments of South Florida, USA:

- The sulfur cycle and carbonate-associated sulfate. In: Amend, J. P., Edwards K. J., and Lyons T. W. (eds.), Sulfur Biogeochemistry Past and Present, Geological Society of America Special Papers, v. 379, p. 161-176.
- Marenco, P. J., 2007, Sulfur isotope geochemistry and the end Permian mass extinction: University of Southern California (Doctoral dissertation), 199 pp.
- Marenco, P. J., Corsetti, F. A., Kaufman, A. J., and Bottjer, D. J., 2008, Environmental and diagenetic variations in carbonate associated sulfate: An investigation of CAS in the Lower Triassic of the western USA: Geochimica et Cosmochimica Acta, v. 72, no. 6, p. 1570-1582.
- Marenco, P. J., Marenco, K. N., Lubitz, R. L., and Niu, D., 2013, Contrasting long-term global and short-term local redox proxies during the Great Ordovician Biodiversification Event: A case study from Fossil Mountain, Utah, USA: Palaeogeography, Palaeoclimatology, Palaeoecology, v. 377, p. 45-51.
- Markovic, S., Paytan, A., and Wortmann, U., 2015, Pleistocene sediment offloading and the global sulfur cycle: Biogeosciences, v. 12, no. 10, p. 3043-3060.
- Markovic, S., Paytan, A., Li, H., and Wortmann, U. G., 2016, A revised seawater sulfate oxygen isotope record for the last 4 Myr: Geochimica et Cosmochimica Acta, v. 175, p. 239-251.
- McLennan, S. M., 2001, Relationships between the trace element composition of sedimentary rocks and upper continental crust: Geochemistry, Geophysics, Geosystems, v. 2, no. 2000GC000109
- Metcalfe, I., Nicoll, R. S., Willink, R., Ladjavadi, M., and Grice, K., 2013, Early Triassic (Induan–Olenekian) conodont biostratigraphy, global anoxia, carbon isotope excursions and environmental perturbations: New data from Western Australian Gondwana: Gondwana Research, v. 23, no. 3, p. 1136-1150.
- Mills, J. V., Antler, G., and Turchyn, A. V., 2016, Geochemical evidence for cryptic sulfur cycling in salt marsh sediments: Earth and Planetary Science Letters, v. 453, p. 23-32.
- Mizutani, Y., and Rafter, T. A., 1969, Oxygen isotopic composition of sulphates. Part 4, Bacterial fractionation of oxygen isotopes in the reduction of sulphate and in the oxidation of sulphur: New Zealand. J. Sci., v. 12, p. 60-68.
- Mizutani, Y., and Rafter, T. A., 1973, Isotopic behaviour of sulphate oxygen in the bacterial reduction of sulphate: Geochemical Journal v. 6, no. 4, p. 183-191.
- Montañez, I. P., Banner, J. L., Osleger, D. A., Borg, L. E., and Bosserman, P. J., 1996, Integrated Sr isotope variations and sea-level history of Middle to Upper Cambrian platform carbonates: Implications for the evolution of Cambrian seawater ⁸⁷Sr/⁸⁶Sr: Geology, v. 24, no. 10, p. 917-920.
- Newton, R. J., Pevitt, E. L., Wignall, P. B., and Bottrell, S. H., 2004, Large shifts in the isotopic composition of seawater sulphate across the Permo–Triassic boundary in northern Italy: Earth and Planetary Science Letters, v. 218, no. 3–4, p. 331-345.
- Orchard, M. J., 2007, Conodont diversity and evolution through the latest Permian and Early Triassic upheavals: Palaeogeography, Palaeoclimatology, Palaeoecology, v. 252, no. 1–2, p. 93-117.
- Orchard, M., and Krystyn, L., 1998, Conodonts of the Lowermost Triassic of Spiti, and New Zonation Based on *Neogondolella Sucessions*: Rivista Italiana di Paleontologia e Stratigrafia, v. 104, no. 3, p. 341-368.

- Payne, J. L., Lehrmann, D. J., Wei, J., Orchard, M. J., Schrag, D. P., and Knoll, A. H., 2004, Large perturbations of the carbon cycle during recovery from the end-Permian extinction: Science, v. 305, no. 5683, p. 506-509.
- Present, T. M., Paris, G., Burke, A., Fischer, W. W., and Adkins, J. F., 2015, Large Carbonate Associated Sulfate isotopic variability between brachiopods, micrite, and other sedimentary components in Late Ordovician strata: Earth and Planetary Science Letters, v. 432, p. 187-198.
- Reichow, M. K., Pringle, M. S., Al'Mukhamedov, A. I., Allen, M. B., Andreichev, V. L., Buslov, M. M., Davies, C. E., Fedoseev, G. S., Fitton, J. G., Inger, S., Medvedev, A. Y., Mitchell, C., Puchkov, V. N., Safonova, I. Y., Scott, R. A., and Saunders, A. D., 2009, The timing and extent of the eruption of the Siberian Traps large igneous province: Implications for the end-Permian environmental crisis: Earth and Planetary Science Letters, v. 277, no. 1–2, p. 9-20.
- Renne, P. R., Zhang, Z., Richards, M. A., Black, M. T., and Basu, A. R., 1995, Synchrony and causal relations between Permian-Triassic boundary crises and Siberian flood volcanism: Science, v. 269, no. 5229, p. 1413.
- Rennie, V. C. F., and Turchyn, A. V., 2014, The preservation of delta $\delta^{34}S_{SO4}$ and delta $\delta^{18}O_{SO4}$ in carbonate-associated sulfate during marine diagenesis: A 25 Myr test case using marine sediments: Earth and Planetary Science Letters, v. 395, p. 13-23.
- Riccardi, A. L., Arthur, M. A., and Kump, L. R., 2006, Sulfur isotopic evidence for chemocline upward excursions during the end-Permian mass extinction: Geochimica et Cosmochimica Acta, v. 70, no. 23, p. 5740-5752.
- Romano, C., Goudemand, N., Vennemann, T. W., Ware, D., Schneebeli-Hermann, E., Hochuli, P. A., Bruhwiler, T., Brinkmann, W., and Bucher, H., 2013, Climatic and biotic upheavals following the end-Permian mass extinction: Nature Geoscience, v. 6, no. 1, p. 57-60.
- Rudnicki, M. D., Elderfield, H., and Spiro, B., 2001, Fractionation of sulfur isotopes during bacterial sulfate reduction in deep ocean sediments at elevated temperatures: Geochimica et Cosmochimica Acta, v. 65, no. 5, p. 777-789.
- Sarmiento, J.Á., Gruber, N., Brzezinski, M.A., Dunne, J.P., 2004. High-latitude controls of thermocline nutrients and low latitude biological productivity. Nature 427, 56-60.
- Schobben, M., Joachimski, M. M., Korn, D., Leda, L., and Korte, C., 2014, Palaeotethys seawater temperature rise and an intensified hydrological cycle following the end-Permian mass extinction: Gondwana Research, v. 26, no. 2, p. 675-683.
- Schobben, M., Stebbins, A., Ghaderi, A., Strauss, H., Korn, D., and Korte, C., 2015, Flourishing ocean drives the end-Permian marine mass extinction: Proceedings of the National Academy of Sciences (U.S.A.), v. 112, no. 33, p. 10298-10303.
- Schobben, M., Stebbins, A., Algeo, T. J., Strauss, H., Leda, L., Haas, J., Struck, U., Korn, D., and Korte, C., 2017, Volatile earliest Triassic sulfur cycle: A consequence of persistent low seawater sulfate concentrations and a high sulfur cycle turnover rate?: Palaeogeography, Palaeoclimatology, Palaeoecology, v. 486, p. 74-85.
- Schoepfer, S. D., Henderson, C. M., Garrison, G. H., Foriel, J., Ward, P. D., Selby, D., Hower, J. C., Algeo, T. J., and Shen, Y., 2013, Termination of a continent-margin upwelling system at the Permian–Triassic boundary (Opal Creek, Alberta, Canada): Global and Planetary Change, v. 105, p. 21-35.

- Sedlacek, A. R. C., Saltzman, M. R., Algeo, T. J., Horacek, M., Brandner, R., Foland, K., and Denniston, R. F., 2014, ⁸⁷Sr/⁸⁶Sr stratigraphy from the Early Triassic of Zal, Iran: Linking temperature to weathering rates and the tempo of ecosystem recovery: Geology, v. 42, no. 9, p. 779-782.
- Shen, J., Schoepfer, S. D., Feng, Q. L., Zhou, L., Yu, J. X., Song, H. Y., Wei, H. Y., and Algeo, T. J., 2015, Marine productivity changes during the end-Permian crisis and Early Triassic recovery: Earth-Science Reviews, v. 149, p. 136-162.
- Shen, J., Feng, Q. L., Algeo, T. J., Li, C., Planaysky, N. J., Zhou, L., and Zhang, M. L., 2016, Two pulses of oceanic environmental disturbance during the Permian-Triassic boundary crisis: Earth and Planetary Science Letters, v. 443, p. 139-152.
- Sinninghe Damsté, J.S., van Bentum, E.C., Reichart, G.J., Pross, J., and Schouten, S., 2010. A CO₂ decrease-driven cooling and increased latitudinal temperature gradient during the mid-Cretaceous Oceanic Anoxic Event 2. Earth and Planetary Science Letters 293, 97-103.
- Sim, M. S., Bosak, T., and Ono, S., 2011, Large sulfur isotope fractionation does not require disproportionation: Science, v. 333, no. 6038, p. 74-77.
- Sobolev, S. V., Sobolev, A. V., Kuzmin, D. V., Krivolutskaya, N. A., Petrunin, A. G., Arndt, N. T., Radko, V. A., and Vasiliev, Y. R., 2011, Linking mantle plumes, large igneous provinces and environmental catastrophes: Nature, v. 477, no. 7364, p. 312-316.
- Song, H. J., Wignall, P. B., Tong, J. N., Bond, D. P. G., Song, H. Y., Lai, X. L., Zhang, K. X., Wang, H. M., and Chen, Y. L., 2012, Geochemical evidence from bio-apatite for multiple oceanic anoxic events during Permian-Triassic transition and the link with end-Permian extinction and recovery: Earth and Planetary Science Letters, v. 353, p. 12-21.
- Song, H. J., Wignall, P. B., Chu, D., Tong, J., Sun, Y., Song, H., He, W., and Tian, L., 2014, Anoxia/high temperature double whammy during the Permian-Triassic marine crisis and its aftermath: Science Reports, v. 4, no. 4132, p. 1-7.
- Song, H. J., Wignall, P. B., Tong, J. N., Song, H. Y., Chen, J., Chu, D. L., Tian, L., Luo, M., Zong, K. Q., Chen, Y. L., Lai, X. L., Zhang, K. X., and Wang, H. M., 2015, Integrated Sr isotope variations and global environmental changes through the Late Permian to early Late Triassic: Earth and Planetary Science Letters, v. 424, p. 140-147.
- Song, H. Y., Tong, J., Algeo, T. J., Horacek, M., Qiu, H., Song, H., Tian, L., and Chen, Z.-Q., 2013, Large vertical $\delta^{13}C_{DIC}$ gradients in Early Triassic seas of the South China craton: Implications for oceanographic changes related to Siberian Traps volcanism: Global and Planetary Change, v. 105, p. 7-20.
- Song, H. Y., Tong, J., Algeo, T. J., Song, H., Qiu, H., Zhu, Y., Tian, L., Bates, S., Lyons, T. W., Luo, G., and Kump, L. R., 2014, Early Triassic seawater sulfate drawdown: Geochimica et Cosmochimica Acta, v. 128, p. 95-113.
- Stanley, S. M., 2009, Evidence from ammonoids and conodonts for multiple Early Triassic mass extinctions: Proceedings of the National Academy of Sciences (U.S.A.), v. 106, no. 36, p. 15264-15267.
- Stebbins, A., Algeo, T. J., Olsen, C., Sano, H., Rowe, H., and Hannigan, R., in review., Sulfur-isotope evidence for recovery of seawater sulfate concentrations from a PTB minimum by the Smithian-Spathian transition: Earth-Science Reviews, in press.
- Stouffer, R.J., Yin, J., Gregory, J.M., Dixon, K.W., Spelman, M.J., Hurlin, W., Weaver, A.J., Eby, M., Flato, G.M., Hasumi, H., Hu, A., Jungclaus, J.H., Kamenkovich, I.V., Levermann, A., Montoya, M., Murakami, S., Nawrath, S., Oka, A., Peltier, W.R.,

- Robitaille, D.Y., Sokolov, A., Vettoretti, G., and Weber, S.L., 2006. Investigating the causes of the response of the thermohaline circulation to past and future climate changes. Journal of Climate 19, 1365-1387.
- Sullivan, L. A., Bush, R. T., and McConchie, D. M., 2000, A modified chromium-reducible sulfur method for reduced inorganic sulfur: optimum reaction time for acid sulfate soil: Australian Journal of Soil Research, v. 38, no. 3, p. 729-734.
- Sun, Y., Joachimski, M. M., Wignall, P. B., Yan, C., Chen, Y., Jiang, H., Wang, L., and Lai, X., 2012, Lethally hot temperatures during the Early Triassic greenhouse: Science, v. 338, no. 6105, p. 366-370.
- Sun, Y., Wignall, P. B., Joachimski, M. M., Bond, D. P. G., Grasby, S. E., Sun, S., Yan, C. B., Wang, L. N., Chen, Y. L., and Lai, X. L., 2015, High amplitude redox changes in the late Early Triassic of South China and the Smithian–Spathian extinction: Palaeogeography, Palaeoclimatology, Palaeoecology, v. 427, p. 62-78.
- Svensen, H., Planke, S., Polozov, A. G., Schmidbauer, N., Corfu, F., Podladchikov, Y. Y., and Jamtveit, B., 2009, Siberian gas venting and the end-Permian environmental crisis: Earth and Planetary Science Letters, v. 277, no. 3–4, p. 490-500.
- Takahashi, S., Yamasaki, S. I., Ogawa, K., Kaiho, K., and Tsuchiya, N., 2015, Redox conditions in the end-Early Triassic Panthalassa: Palaeogeography Palaeoclimatology Palaeoecology, v. 432, p. 15-28.
- Takano, B., 1985, Geochemical implications of sulfate in sedimentary carbonates: Chemical Geology, v. 49, no. 4, p. 393-403.
- Tian, L., Tong, J. N., Algeo, T. J., Song, H. J., Song, H. Y., Chu, D. L., Shi, L., and Bottjer, D. J., 2014, Reconstruction of Early Triassic ocean redox conditions based on framboidal pyrite from the Nanpanjiang Basin, South China: Palaeogeography Palaeoclimatology Palaeoecology, v. 412, p. 68-79.
- Turchyn, A. V., and Schrag, D. P., 2006, Cenozoic evolution of the sulfur cycle: Insight from oxygen isotopes in marine sulfate: Earth and Planetary Science Letters, v. 241, no. 3–4, p. 763-779.
- Turchyn, A. V., Schrag, D. P., Coccioni, R., and Montanari, A., 2009, Stable isotope analysis of the Cretaceous sulfur cycle: Earth and Planetary Science Letters, v. 285, no. 1–2, p. 115-123.
- Ware, D., Bucher, H., Brayard, A., Schneebeli-Hermann, E., and Brühwiler, T., 2015, High-resolution biochronology and diversity dynamics of the Early Triassic ammonoid recovery: The Dienerian faunas of the Northern Indian Margin: Palaeogeography, Palaeoclimatology, Palaeoecology, v. 440, p. 363-373.
- Wei, H., Algeo, T. J., Yu, H., Wang, J. G., Guo, C., and Shi, G., 2015a, Episodic euxinia in the Changhsingian (late Permian) of South China: Evidence from framboidal pyrite and geochemical data: Sedimentary Geology, v. 319, p. 78-97.
- Wei, H., Shen, J., Schoepfer, S. D., Krystyn, L., Richoz, S., and Algeo, T. J., 2015b, Environmental controls on marine ecosystem recovery following mass extinctions, with an example from the Early Triassic: Earth-Science Reviews, v. 149, p. 108-135.
- Whitney, F.A., Crawford, W.R., and Harrison, P.J., 2005. Physical processes that enhance nutrient transport and primary productivity in the coastal and open ocean of the subarctic NE Pacific. Deep Sea Research Part II: Topical Studies in Oceanography 52, 681-706.
- Wignall, P. B., 2001, Large igneous provinces and mass extinctions: Earth-Science Reviews, v. 53, no. 1–2, p. 1-33.

- Wignall, P. B., Bond, D. P. G., Kuwahara, K., Kakuwa, Y., Newton, R. J., and Poulton, S. W., 2010, An 80 million year oceanic redox history from Permian to Jurassic pelagic sediments of the Mino-Tamba terrane, SW Japan, and the origin of four mass extinctions: Global and Planetary Change, v. 71, no. 1-2, p. 109-123.
- Wignall, P. B., Bond, D. P. G., Sun, Y., Grasby, S. E., Beauchamp, B., Joachimski, M. M., and Blomeier, D. P. G., 2015, Ultra-shallow-marine anoxia in an Early Triassic shallow-marine clastic ramp (Spitsbergen) and the suppression of benthic radiation: Geological Magazine, v. 153, no. 2, p. 316-331.
- Wilkin, R., Barnes, H., and Brantley, S., 1996, The size distribution of framboidal pyrite in modern sediments: An indicator of redox conditions: Geochimica et Cosmochimica Acta, v. 60, no. 20, p. 3897-3912.
- Worden, R. H., Smalley, P. C., and Fallick, A. E., 1997, Sulfur cycle in buried evaporites: Geology, v. 25, no. 7, p. 643-646.
- Wortmann, U. G., Bernasconi, S. M., and B tcher, M. E., 2001, Hypersulfidic deep biosphere indicates extreme sulfur isotope fractionation during single-step microbial sulfate reduction: Geology, v. 29, no. 7, p. 647-650.
- Wortmann, U. G., Chernyavsky, B., Bernasconi, S. M., Brunner, B., Böttcher, M. E., and Swart, P. K., 2007, Oxygen isotope biogeochemistry of pore water sulfate in the deep biosphere: Dominance of isotope exchange reactions with ambient water during microbial sulfate reduction (ODP Site 1130): Geochimica et Cosmochimica Acta, v. 71, no. 17, p. 4221-4232.
- Wotte, T., Shields-Zhou, G. A., and Strauss, H., 2012, Carbonate-associated sulfate: Experimental comparisons of common extraction methods and recommendations toward a standard analytical protocol: Chemical Geology, v. 326, p. 132-144.
- Zhang, F.F., Romaniello, S.J., Algeo, T.J., Lau, K.V., Clapham, M.E., Richoz, S., Herrmann, A.D., Smith, H., and Anbar, A.D., 2018. Multiple episodes of extensive oceanic anoxia linked to global warming and continental weathering following the latest Permian mass extinction. Science Advances, v. 4, no. 4, e1602921.
- Zhang, L., Zhao, L., Chen, Z. Q., Algeo, T. J., Chen, J., Wang, R., Chen, L., Hou, J., Li, Y., Qiu, H., Feng, X., Lu, Z., Wang, X., and Huang, Y., 2014, Amelioration of marine environments at the Smithian–Spathian boundary, Early Triassic: Biogeosciences, v. 12, no. 5, p. 1597-1613.
- Zhang, L., Orchard, M. J., Brayard, A., Algeo, T. J., Zhao, L., Chen, Z.-Q., in review, The Smithian-Spathian boundary (late Early Triassic): a review and proposed definition: Earth-Science Reviews, in review.